Stefan Pachmajer, BSc

Feasibility study for the observation of the inverse piezoelectric effect by X-ray diffraction

MASTER THESIS

for obtaining the academic degree
Diplom-Ingenieur

Master Programme of
Technical Physics

Graz University of Technology

Supervisor:
Ao.Univ.-Prof. Dipl.-Ing. Dr.techn. Roland Resel
Institute of Solid State Physics
Graz University of Technology

Graz, May 2014

Deutsche Fassung:
Beschluss der Curricula-Kommission für Bachelor-, Master- und Diplomstudien vom 10.11.2008
Genehmigung des Senates am 1.12.2008

EIDESSTATTLICHE ERKLÄRUNG

Ich erkläre an Eides statt, dass ich die vorliegende Arbeit selbstständig verfasst, andere als die angegebenen Quellen/Hilfsmittel nicht benutzt, und die den benutzten Quellen wörtlich und inhaltlich entnommene Stellen als solche kenntlich gemacht habe.

Graz, am …… ……..
(Unterschrift)

Englische Fassung:

STATUTORY DECLARATION

I declare that I have authored this thesis independently, that I have not used other than the declared sources / resources, and that I have explicitly marked all material which has been quoted either literally or by content from the used sources.

…… ……..
date (signature)

Acknowledgement

Foremost, I would like to express my gratitude to my supervisor Roland Resel for the possibility of being part of his working group and his continuous support. Specifically the various travels to conferences and synchrotrons were a great experience for me.

My special thanks are extended to the whole group, consisting of Reinhold Hetzel, Christian Röthel, Michael Zawodzki, Katrin Unger, Christoph Lercher, Alexander Pichler and Andrew Jones. Thank you all for helping me to maneuver the red line through my work, sharing an office with me and being so much more than only colleagues.

Apart from our group I would like to thank all the people from the Institute of Solid State Physics, especially Bettina Friedel for introducing me to the lab and helping me with my samples. Also the assistance provided by Birgit Kunert, Elisabeth Stern and Harald Kerschbaumer was greatly appreciated.

I would also like to thank the following people for providing me samples and their knowledge and thus making this work possible: Adele Sassella from University of Milano-Bicocca, for providing me samples of KAP. Christof Zarfl from Piezocryst, Austria, who supported me with samples of $GaPO_4$. Martin Zirkl from Joanneum Research, Austria, who assisted me with P(VDF:TrFE).

I would also especially like to thank my parents for their unconditional support and the night long philosophical discussions which I particularly enjoyed and always have been a motivating force to me. Last but by no means least I would like to thank my better half Lara Köck for her great patience and being my major support. Thank you for accompanying me on this adventure, I look forward to our next one!

Abstract

X-ray crystallography has always been a fundamental tool in many scientific fields. This is hardly surprising as one can gain a lot of fundamental information on investigated materials like crystal structures, chemical bondings or electron densities. It is therefore evident, that the techniques are improved continuously. One of the main parts of every X-ray diffractometer is the sample stage, which is nowadays much more than only a table to fix a sample. This work concentrates on measurements using a new kind of sample stage which provides the possibility to apply an external electric field while performing X-ray scattering experiments.

Electrostriction, piezo-, pyro- and ferroelectricity describe electromechanical couplings showing slightly different phenomena. Measuring such materials in an X-ray diffractometer one can expect changes of 10^{-3} to 10^{-4° in scattering angle 2θ by applying an electric field with a field strength of up to $10^6\,V/\mathrm{m}$. The piezoelectric effect of Gallium orthophosphate was investigated. Calculations let expect changes of $8 \cdot 10^{-4^\circ}$ at a scattering angle of 141° 2θ. Even though the effect is minute, measurements show a clear trend and delivered a piezoelectric constant of $d_{11} = 14\,pm/\mathrm{V}$ compared to a literature value of $d_{11} = 4.5\,pm/\mathrm{V}$. Potassium hydrogen phthalate as organic representative of piezoelectric materials revealed an electrostrictive-like behavior. With an electric field across its (010) plane, a shear strain in yz-direction was expected leading to a change of $\Delta\theta = 0.0008^\circ$. Electrostriction superimposed this expectation and an electrostrictive coefficient of $M_{22} = -5.05 \times 10^{-17}\,C^2/\mathrm{N}^2$ was determined from measurements. Polyvinylidenefluorid-trifluoroethylene (P(VDF:TrFE)) with its ferroelectric-paraelectric phase transition is finally used to point out capabilities of combined stages. The material was heated up to its critical point at roughly 80°C and by applying an external voltage it is shown that this point can be reversibly moved within a small range of some degree Celsius. For P(VDF:TrFE) 70:30 the Clausius-Clapeyron relation delivers a theoretical value of $\left(\partial T_c/\partial E\right)_p = 2.7 \times 10^{-7}\,Km/\mathrm{V}$ for this shift while experiments delivered a value of $1.5 \times 10^{-7}\,Km/\mathrm{V}$.

Kurzfassung

Kristallstrukturanalyse ist seit jeher ein grundlegendes Werkzeug in vielen wissenschaftlichen Bereichen. Dies ist angesichts der fundamentalen Informationen, die man über die untersuchten Materialien gewinnen kann, kaum verwunderlich. Es ist daher naheliegend, Methoden und Geräte kontinuierlich zu verbessern. Einer der wichtigsten Teile eines jeden Röntgendiffraktometer ist die Probenbühne, heutzutage wesentlich mehr als nur eine einfache Platte. Diese Arbeit konzentriert sich auf Messungen mit einer neuen Art Probenbühne, welche die Möglichkeit bietet, zeitgleich zu einer Röntgenmessung ein externes elektrisches Feld an der untersuchten Probe anzulegen. Elektrostriktion, Piezo-, Pyro- und Ferroelektrizität beschreiben elektromechanische Kopplungen mit leicht unterschiedlichen Phänomenen. In einem Röntgendiffraktometer vermessen können durch Anlegen einer Spannung Änderungen im Größenbereich von 10^{-3} bis 10^{-4° im Streuwinkel 2θ erwartet werden. Der Piezoelektrische Effekt von Gallium Orthophosphat wurde untersucht. Erste Berechnungen ließen Änderungen von $8 \cdot 10^{-4^\circ}$ bei einem Streuwinkel von 141° 2θ erwarten. Auch wenn das Material nur kleine Effekte zeigt, lieferte es Messungen mit einem klaren Trend und eine piezoelektrische Konstante von $d_{11} = 14\,^{pm}/_{\mathrm{V}}$ konnte berechnet werden. Die Literatur liefert hierfür einen Wert von $d_{11} = 4.5\,^{pm}/_{\mathrm{V}}$. Kaliumhydrogenphthalat als organischer Vertreter von piezoelektrischen Materialien zeigte elektrostriktiv-typisches Verhalten. Mit einem elektrischen Feld normal zur (010) Ebene wurde eine Scherspannung in yz-Richtung erwartet und eine Änderung von $\Delta\theta = 0.0008^\circ$ berechnet. Elektrostriktion überlagerte diesen Effekt und ein elektrostriktiver Koeffizient von $M_{22} = -5.05 \times 10^{-17}\,^{C^2}/_{\mathrm{N}^2}$ konnte aus den Messungen heraus bestimmt werden. Polyvinylidenefluorid-Trifluoroethylen (P(VDF:TrFE)) mit seinem ferroelektrischen-paraelektrischen Phasenübergang wurde schließlich verwendet um Kombinationsmöglichkeiten mit anderen Probebühnen aufzuzeigen. Das Material wurde bis zu seinem kritischen Punkt bei circa 80°C erwärmt wo durch Anlegen einer Spannung nachgewiesen wurde, dass dieser Punkt reversibel in einem kleinen Temperaturbereich verändert werden kann. Für P(VDF:TrFE) 70:30 liefert die Clausius-Clapeyron Relation einen theoretischen Wert von $\left(\partial T_c/\partial E\right)_p = 2.7 \times 10^{-7}\,^{Km}/_{\mathrm{V}}$ für diesen Shift. Experimente lieferten einen Wert von $1.5 \times 10^{-7}\,^{Km}/_{\mathrm{V}}$.

Contents

1 Introduction

1.1 X-ray diffraction

Since the first days of X-ray crystallography around 1912, its potential on determining crystal structures has been known. It became a principal method and was therefore always of interest to be further developed. While different X-ray techniques like powder diffraction, single crystal diffraction or small angle X-ray diffraction have been worked out, it was long time a static measurement. By inventing brighter X-ray sources, more sensible detection systems and improved attachments, in-situ measurements became possible. Therefore different kinds of sample stages have been developed like heating stages, humidity chambers or tensile stages. As many materials react somehow on external electric fields, a new kind of stage is proven on its feasibilities in this work. This electric stage is able to apply an electric field across a measured sample in-situ thus expanding the field of available sample stages for X-ray diffractometers.

1.2 Sample stage with electrical contacts

A figure of the used electric stage is given with 1.1. The stage is mountable on most four-circle-goniometer and XYZ stages with according fitting plates. In the middle a plastic socket of $20 \times 20\,\mathrm{mm}^2$ provides space for standard wafer sizes and prevents direct electric contact with the stage body. On the outside, six BNC connectors are available to connect an external voltage source. From the connectors small cables are drawn through the stage to the electric contacts next to the sample socket. These contacts are sitting on a magnetic base for higher stability. Contact arms can be adjusted to the sample height with small screws. In addition an inert gas port is available for measurements under inert gas

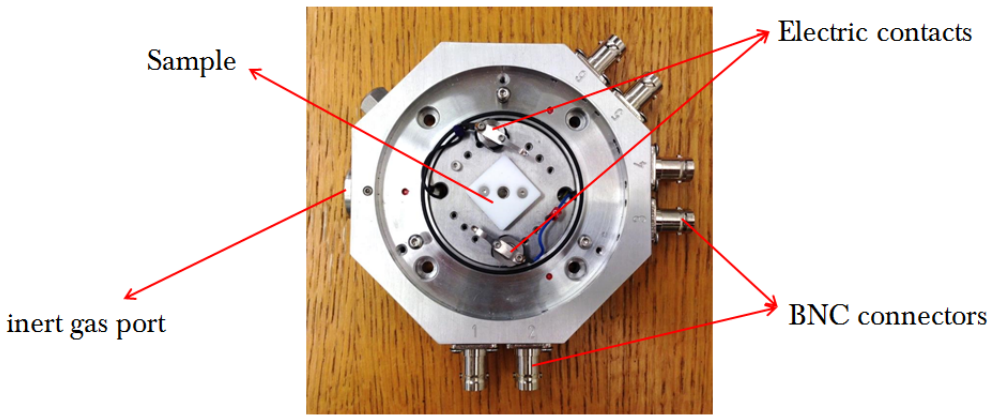

Figure 1.1: Sample stage with electric contacts for in-situ measurements.

atmosphere. To do so, a graphite and a plastic dome are part of the attachment but are not shown on the picture. If the electric contacts are not enough to fix a sample, additional contacts working like clamps can be used to prevent unintended sample movements.

To be able to measure changes through an external electric field, samples have to be prepared. Figure 1.2 shows a schematic drawing of a prepared sample. As basis a wafer with a conductive layer (here gold is used as representative) is needed to establish electric contact with the sample bottom electrode. The sample itself should be attached with a bottom and top electrode to guarantee a linear electric field inside the sample. Also the positions for the electric contacts, the resulting electric field direction, direction of the beam and the interplanar distance d are shown. The interplay of direction of electric field, measurement direction and the materials orientation on the wafer determines the resulting effect.

1.3 Piezo- and ferroelectric materials

The materials used in this work exhibit piezo- and/or ferroelectric properties. These electromechanical couplings are well suited for the purpose of testing an electric sample stage. In general piezoelectric materials are build in stacks to

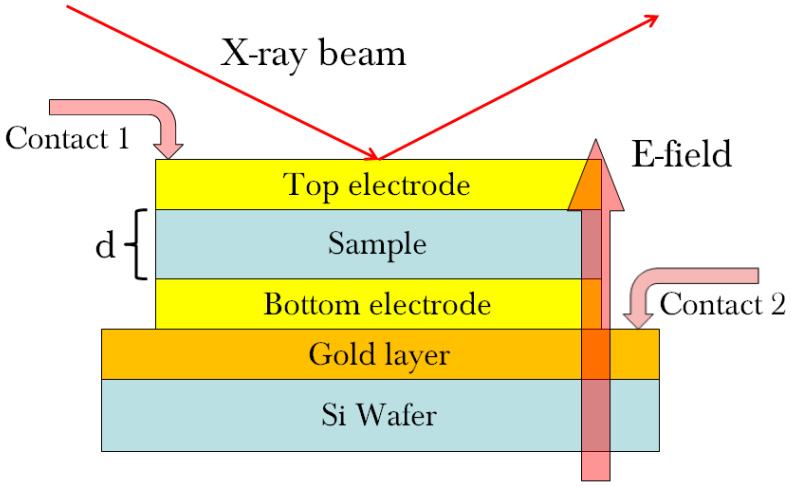

Figure 1.2: Conditions on samples for use with electric sample stage.

enlarge the size-changing effect. This requires complex production steps and is therefore as sample source not preferred. With X-ray diffraction small changes in interplanar distance d_{hkl} become measurable and already simple, one layered samples of a piezoelectric material are suited to be measured.

As inorganic material, gallium orthophosphate ($GaPO_4$) was chosen. Very similar to quartz, but in comparison to it, it is a quite temperature-stable material mainly used in pressure sensors in high temperature environments. As it has no natural origin, it has to be grown synthetically, which is done by the company Piezocryst, Austria. Potassium hydrogen phthalate is often used in chemistry for different purposes. Its ten times higher piezoelectric coefficients compared to gallium orthophosphate makes it interesting for the aims of this work. Polyvinylidenefluoride-trifluoroethylene finally is a ferroelectric representative. The polymer polyvinylidenefluoride is due to its thermal and chemical stability a widely used material in very different kinds of applications. Its copolymer with trifluoroethylene becomes more and more interesting as it forms a stable ferroelectric phase at room temperature. It is therefore used as printable heat

and pressure sensor. A phase transition occurs before melting and the effects of an external electric field on this phase transition are studied.

2 Theory fundamentals

2.1 Piezoelectric effect

Piezoelectricity is defined by the Oxford Dictionaries as "electric polarization in a substance (especially certain crystals) resulting from the application of mechanical stress." [1]. More precisely this polarization is proportional to the strain and changes its sign with it. This statement describes the direct piezoelectric effect. Its inversion is called inverse piezoelectric effect, whereby a piezoelectric crystal becomes strained under an external electric field by an amount proportional to this field. Figure 2.1 shows this behavior schematically with the resulting net dipole in the middle. The most left picture shows the material without external electric field and net polarization equals zero. By applying an external electric field the molecules gain electric dipole moment depending on the direction of the field (middle and most right picture). This movement has a magnitude of about one atomic distance. It is obvious, that a mechanical deformation can only happen when the net dipole is different to zero in an external electric field. This is true for noncentrosymmetric crystals. This linear electromechanical coupling is described by a rank three tensor:

$$P_i = d_{ijk}\,\sigma_{jk} \qquad (i,j,k = 1,2,3) \tag{2.1}$$

for the direct piezoelectric effect and

$$\epsilon_{jk} = d_{ijk}\,E_i \qquad (i,j,k = 1,2,3) \tag{2.2}$$

($\boldsymbol{P}$ - polarization, $\boldsymbol{\sigma}$ - 2nd rank stress tensor, $\boldsymbol{\epsilon}$ - 2nd rank strain tensor, $\boldsymbol{d}$ - 3rd rank tensor for piezoelectric coefficients) for the indirect piezoelectric effect with the Einstein summation convention to be applied [2]. Both equations are coupled

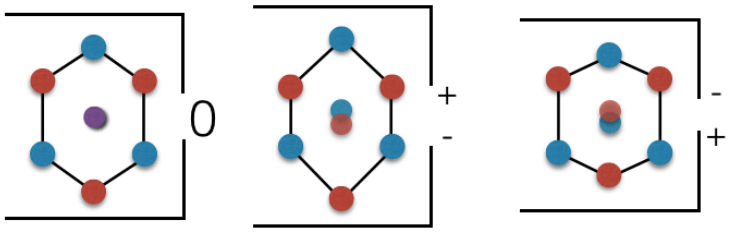

Figure 2.1: Inverse piezoelectric effect: strained piezoelectric crystal due to polarization caused by an external electric field. The effect goes linear and proportional with the polarizing field.

with the same piezoelectric coefficient matrix, a rank three tensor, which would result in 27 elements for the piezoelectric coefficients. However stress and strain tensors are symmetric ones and their indices can be therefore relabeled in the following way: $11 \rightarrow 1; 22 \rightarrow 2; 33 \rightarrow 3; 23 \rightarrow 4; 13 \rightarrow 5; 12 \rightarrow 6$ [3]. This reduces the piezoelectric coefficients to 18 elements. In order to illustrate this, one can apply for example a shear stress σ_{12} on a sample. As it is obvious out of figure 2.2, to be in static equilibrium, σ_{jk} has to be equal σ_{kj}, otherwise a rotation of the sample would take place. For the example this results in a total polarization of

$$P_i = d_{i12}\sigma_{12} + d_{i21}\sigma_{21} = (d_{i12} + d_{i21})\sigma_{12} \tag{2.3}$$

A separated determination of d_{ijk} and d_{ikj} is therefore not possible and makes a reduction of indices possible.
The indices of the stress tensor (the same holds for the strain tensor indices) get reduced in the following way:

$$\sigma_n = \begin{bmatrix} \sigma_{11} & \sigma_{12} & \sigma_{13} \\ \sigma_{21} & \sigma_{22} & \sigma_{23} \\ \sigma_{31} & \sigma_{32} & \sigma_{33} \end{bmatrix} = \begin{bmatrix} \sigma_1 & \sigma_6 & \sigma_5 \\ \sigma_6 & \sigma_2 & \sigma_4 \\ \sigma_5 & \sigma_4 & \sigma_3 \end{bmatrix} \tag{2.4}$$

Together with the piezoelectric coefficients

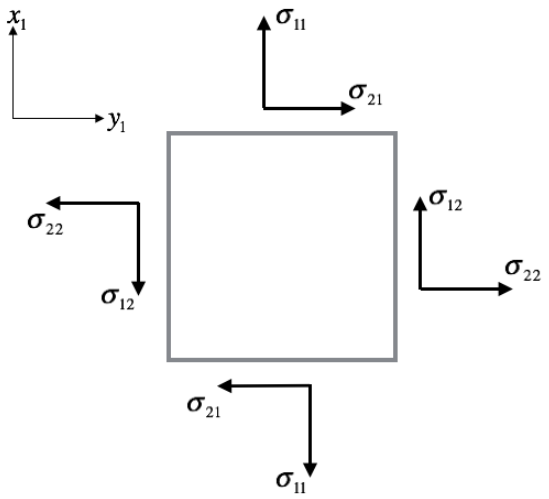

Figure 2.2: Directions for stresstensor elements. $\sigma_{jk} \neq \sigma_{kj}$ would cause a sample rotation.

$$d_{mn} = \begin{bmatrix} d_{11} & d_{12} & d_{13} & d_{14} & d_{15} & d_{16} \\ d_{21} & d_{22} & d_{23} & d_{24} & d_{25} & d_{26} \\ d_{31} & d_{32} & d_{33} & d_{34} & d_{35} & d_{36} \end{bmatrix} \tag{2.5}$$

where the first 9 elements from d_{11} to d_{33} describe reactions on normale stress and the second 9 elements from d_{24} to d_{36} describe reactions on shear stress, equation (2.1) becomes

$$P_m = d_{mn}\,\sigma_n \qquad (m = 1, 2, 3; n = 1, ..., 6;) \tag{2.6}$$

and the same way equation (2.2) becomes

$$\epsilon_n = d_{mn}\,E_m \qquad (m = 1, 2, 3; n = 1, ..., 6;) \tag{2.7}$$

That the same piezoelectric coefficients apply to both equations can also be shown by their unit. Polarization is given in $^{C}/_{m^2}$, stress is given in $^{N}/_{m^2}$. Therefore the piezoelectric coefficients must be given in $^{C}/_{N}$. The electric field has the unit $^{V}/_{m}$. To derive the dimensionless strain tensor, the piezoelectric coefficients in this case must be $^{m}/_{V}$. A conversion from $^{C}/_{N}$ to $^{m}/_{V}$ is easily derived:

$$1\,\frac{\mathrm{C}}{\mathrm{N}} = 1\,\frac{\mathrm{As}}{\mathrm{N}} = 1\,\frac{\mathrm{Ws}}{\mathrm{VN}} = 1\,\frac{\mathrm{kgm}^2}{\mathrm{s}^2\mathrm{VN}} = 1\,\frac{\mathrm{kgm}^2\mathrm{s}^3}{\mathrm{kgms}^3\mathrm{V}} = 1\,\frac{\mathrm{m}}{\mathrm{V}} \tag{2.8}$$

Most important property for a material to show a piezoelectric effect is the lack of an inversion center. In case of centrosymmetric crystals, there is a indistinguishable point (-x,-y,-z) for every point (x,y,z) in the unit cell and dipoles would always cancel each other out. To polarize a material, non-centrosymmetricity is necessary. Of the overall 32 crystal classes, 21 are non-centrosymmetric and 20 of these have piezoelectric constants different from zero. Table 2.1.1 lists them up [4].

2.1.1 Determination of piezoelectric coefficients by common methods

X-ray diffraction is in general not the first choice to determine a piezoelectric coefficient matrix. More common are the frequency method, the laser interferometry method and the quasi-static method. The first method measures a materials impedance and resonance frequencies to be able to calculate the piezoelectric matrix according to the European standard EN 50324-2 [5]. Laser interferometry measures deflections on samples and their deviations due to applied electric fields. This sets high requirements on the construction as even smallest vibrations during a measurement significantly influence the results. The last method mentioned is based on the direct piezoelectric effect. A constant force is brought onto the sample and with an oscilloscope appearing voltages are measured. Out of the relationship of force F and voltage U, the piezoelectric constants can be calculated. For further information to all three methods, the gentle reader may be referred to [6].

Table 2.1: Piezoelectric crystal classes with accompanying third rank tensors describing the positions and values of piezoelectric coefficients.

Crystal system	**Crystal class**	**Int. symbol**	**Third rank tensor**
Triclinic $a \neq b \neq c$ $\alpha \neq \beta \neq \gamma$	triclinic-pedial	1	$\begin{bmatrix} d_{11} & d_{12} & d_{13} & d_{14} & d_{15} & d_{16} \\ d_{21} & d_{22} & d_{23} & d_{24} & d_{25} & d_{26} \\ d_{31} & d_{32} & d_{33} & d_{34} & d_{35} & d_{36} \end{bmatrix}$
Monoclinic $a \neq b \neq c$ $\alpha \neq 90^\circ$ $\beta = \gamma = 90^\circ$	monoclinic-sphenoidal	2	$\begin{bmatrix} 0 & 0 & 0 & d_{14} & d_{15} & 0 \\ 0 & 0 & 0 & d_{24} & d_{25} & 0 \\ d_{31} & d_{32} & d_{33} & 0 & 0 & d_{36} \end{bmatrix}$
	monoclinic-domatic	m	$\begin{bmatrix} d_{11} & d_{12} & d_{13} & 0 & 0 & d_{16} \\ d_{21} & d_{22} & d_{23} & 0 & 0 & d_{26} \\ 0 & 0 & 0 & d_{34} & d_{35} & 0 \end{bmatrix}$
Orthorhombic $a \neq b \neq c$ $\alpha = \beta = \gamma = 90^\circ$	orthorhombic-disphenoidal	222	$\begin{bmatrix} 0 & 0 & 0 & d_{14} & 0 & 0 \\ 0 & 0 & 0 & 0 & d_{25} & 0 \\ 0 & 0 & 0 & 0 & 0 & d_{36} \end{bmatrix}$
	orthorhombic-pyramidal	mm2	$\begin{bmatrix} 0 & 0 & 0 & 0 & d_{15} & 0 \\ 0 & 0 & 0 & d_{24} & 0 & 0 \\ d_{31} & d_{32} & d_{33} & 0 & 0 & 0 \end{bmatrix}$
Tetragonal $a \neq c$	tetragonal-pyramidal	4	$\begin{bmatrix} 0 & 0 & 0 & d_{14} & d_{15} & 0 \\ 0 & 0 & 0 & d_{15} & -d_{14} & 0 \\ d_{31} & d_{31} & d_{33} & 0 & 0 & 0 \end{bmatrix}$
	tetragonal-disphenoidal	$\bar{4}$	$\begin{bmatrix} 0 & 0 & 0 & d_{14} & d_{15} & 0 \\ 0 & 0 & 0 & -d_{15} & d_{14} & 0 \\ d_{31} & -d_{31} & 0 & 0 & 0 & d_{36} \end{bmatrix}$
	tetragonal-trapezoidal	422	$\begin{bmatrix} 0 & 0 & 0 & d_{14} & 0 & 0 \\ 0 & 0 & 0 & 0 & -d_{14} & 0 \\ 0 & 0 & 0 & 0 & 0 & 0 \end{bmatrix}$
	ditetragonal-pyramidal	4mm	$\begin{bmatrix} 0 & 0 & 0 & 0 & d_{15} & 0 \\ 0 & 0 & 0 & d_{15} & 0 & 0 \\ d_{31} & d_{31} & d_{33} & 0 & 0 & 0 \end{bmatrix}$
	tetragonal-scalenoidal	$\bar{4}$2m	$\begin{bmatrix} 0 & 0 & 0 & d_{14} & 0 & 0 \\ 0 & 0 & 0 & 0 & d_{14} & 0 \\ 0 & 0 & 0 & 0 & 0 & d_{36} \end{bmatrix}$

Crystal system	**Crystal class**	**Int. symbol**	**Third rank tensor**
Trigonal $\alpha, \beta, \gamma \neq 90^\circ$	trigonal-pyramidal	3	$\begin{bmatrix} d_{11} & -d_{11} & 0 & d_{14} & d_{15} & d_{21} \\ d_{21} & -d_{21} & 0 & d_{15} & -d_{14} & -d_{11} \\ d_{31} & d_{31} & d_{33} & 0 & 0 & 0 \end{bmatrix}$
	trigonal-trapezoidal	32	$\begin{bmatrix} d_{11} & -d_{11} & 0 & d_{14} & 0 & 0 \\ 0 & 0 & 0 & 0 & -d_{14} & -d_{11} \\ 0 & 0 & 0 & 0 & 0 & 0 \end{bmatrix}$
	ditrigonal-pyramidal	3m	$\begin{bmatrix} 0 & 0 & 0 & 0 & d_{15} & d_{21} \\ d_{21} & -d_{21} & 0 & d_{15} & 0 & 0 \\ d_{31} & d_{31} & d_{33} & 0 & 0 & 0 \end{bmatrix}$
Hexagonal $a \neq c$	hexagonal-pyramidal	6	$\begin{bmatrix} 0 & 0 & 0 & d_{14} & d_{15} & 0 \\ 0 & 0 & 0 & d_{15} & -d_{14} & 0 \\ d_{31} & d_{31} & d_{33} & 0 & 0 & 0 \end{bmatrix}$
	trigonal-dipyramidal	$\bar{6}$	$\begin{bmatrix} d_{11} & -d_{11} & 0 & 0 & 0 & d_{21} \\ d_{21} & -d_{21} & 0 & 0 & 0 & -d_{11} \\ 0 & 0 & 0 & 0 & 0 & 0 \end{bmatrix}$
	hexagonal-trapezoidal	622	$\begin{bmatrix} 0 & 0 & 0 & d_{14} & 0 & 0 \\ 0 & 0 & 0 & 0 & -d_{14} & 0 \\ 0 & 0 & 0 & 0 & 0 & 0 \end{bmatrix}$
	dihexagonal-pyramidal	6mm	$\begin{bmatrix} 0 & 0 & 0 & 0 & d_{15} & 0 \\ 0 & 0 & 0 & d_{15} & 0 & 0 \\ d_{31} & d_{31} & d_{33} & 0 & 0 & 0 \end{bmatrix}$
	ditrigonal-dipyramidal	$\bar{6}$m2	$\begin{bmatrix} 0 & 0 & 0 & 0 & 0 & d_{21} \\ d_{21} & -d_{21} & 0 & 0 & 0 & 0 \\ 0 & 0 & 0 & 0 & 0 & 0 \end{bmatrix}$
Cubic	tetrahedral	23	$\begin{bmatrix} 0 & 0 & 0 & d_{36} & 0 & 0 \\ 0 & 0 & 0 & 0 & d_{36} & 0 \\ 0 & 0 & 0 & 0 & 0 & d_{36} \end{bmatrix}$
	hextetrahedral	$\bar{4}$3m	$\begin{bmatrix} 0 & 0 & 0 & d_{36} & 0 & 0 \\ 0 & 0 & 0 & 0 & d_{36} & 0 \\ 0 & 0 & 0 & 0 & 0 & d_{36} \end{bmatrix}$

2.1.2 Determination of piezoelectric coefficients by X-ray diffraction

Because the macroscopic deformations of piezoelectric crystals have their origin in microscopic deformations of the unit cell, X-ray diffraction offers a direct way to measure piezoelectric constants from the changes of Bragg-peak positions in the diffraction pattern. The well known Bragg equation for constructive interference of an incident X-ray beam with wavelength λ is given by

$$n\lambda = 2d_{hkl}\sin\theta \tag{2.9}$$

where θ is the incident beam angle and d_{hkl} describes the interplanar spacing between lattice planes. The latter is connected to a reciprocal lattice vector by

$$\frac{2\pi}{d_{hkl}} = G_{hkl} = \sqrt{\boldsymbol{G}_{hkl}\cdot\boldsymbol{G}_{hkl}} \tag{2.10}$$

where

$$\boldsymbol{G}_{hkl} = h\boldsymbol{a^*} + k\boldsymbol{b^*} + l\boldsymbol{c^*} \tag{2.11}$$

with reciprocal lattice base vectors $\boldsymbol{a^*}$,$\boldsymbol{b^*}$ and $\boldsymbol{c^*}$. From the base vectors of the real lattice the reciprocal lattice can be calculated by:

$$\begin{aligned}\boldsymbol{a^*} &= \frac{2\pi}{V}\cdot\boldsymbol{b}\times\boldsymbol{c}\\ \boldsymbol{b^*} &= \frac{2\pi}{V}\cdot\boldsymbol{a}\times\boldsymbol{c}\\ \boldsymbol{c^*} &= \frac{2\pi}{V}\cdot\boldsymbol{a}\times\boldsymbol{b}\end{aligned} \tag{2.12}$$

with V, the Volume of the unit cell. One can write down the unit cell vectors for the direct and reciprocal lattice as matrices

$$A = \begin{pmatrix} a_1 & b_1 & c_1\\ a_2 & b_2 & c_2\\ a_3 & b_3 & c_3\end{pmatrix}, A^* = \begin{pmatrix} a_1^* & b_1^* & c_1^*\\ a_2^* & b_2^* & c_2^*\\ a_3^* & b_3^* & c_3^*\end{pmatrix} \tag{2.13}$$

Equation (2.7) gives the correlation between an external electric field and an induced elastic strain $\boldsymbol{\epsilon}$. This strain changes the base vectors according to [7]:

$$\boldsymbol{A(\epsilon)} = (\boldsymbol{I} + \boldsymbol{\epsilon})\boldsymbol{A(0)} \tag{2.14}$$

Matrix A(0) describes the unit cell vectors without strain while A(ϵ) describes the base vectors with corresponding strain. I is the unity matrix. The same equation holds for the reciprocal space. Applied to the reciprocal lattice vectors in the Bragg equation, it can be shown that the Bragg angle θ changes by $\Delta\theta$ [8]:

$$\Delta\theta = -E \tan\theta \sum_{i=1}^{3}\sum_{j=1}^{3}\sum_{k=1}^{3} e_i\, h_j\, h_k\, d_{ijk} \tag{2.15}$$

with

$$\boldsymbol{h} = \frac{\boldsymbol{G_{hkl}}}{G_{hkl}}$$

and e_i, the direction cosine of the electric field. What appears to be quite complicated in the first moment becomes clear when one reminds what was mentioned before according the piezoelectric components. The first index i in d_{ijk} gives the direction of the electric field (or applied stress in the direct effect) and e_i describes therefore how strong a general electric field is in this certain direction. The indices j and k describe the direction of reaction. Normal reactions appear if j equals k, shear reactions if j is different to k. The amount of reaction must be connected to an interplanar distance d, which is done via the normalized reciprocal lattice vector $\boldsymbol{h}$ describing how strong this vector is changed in a certain direction. Figure 2.3 illustrates this behavior between interplanar distance d and a Bragg shift schematically. A smaller distance d leads to peaks at higher angles while a broadening of the material, resulting in wider interplanar distance d leads to peaks at lower diffraction angles. As the change in the diffraction angle θ goes with its tangent in equation (2.15) it is obvious that measurements at higher angles lead to bigger changes. They can be expected in the order of $\Delta\theta = 10^{-4^\circ}$ to 10^{-3°, which makes it absolutely necessary to measure at high angles for materials with low piezoelectric coefficients. Application of equation (2.15) to the piezoelectric crystal classes in table 2.1.1 leads to specific equations and allows to determine in which directions a sample has to be measured to

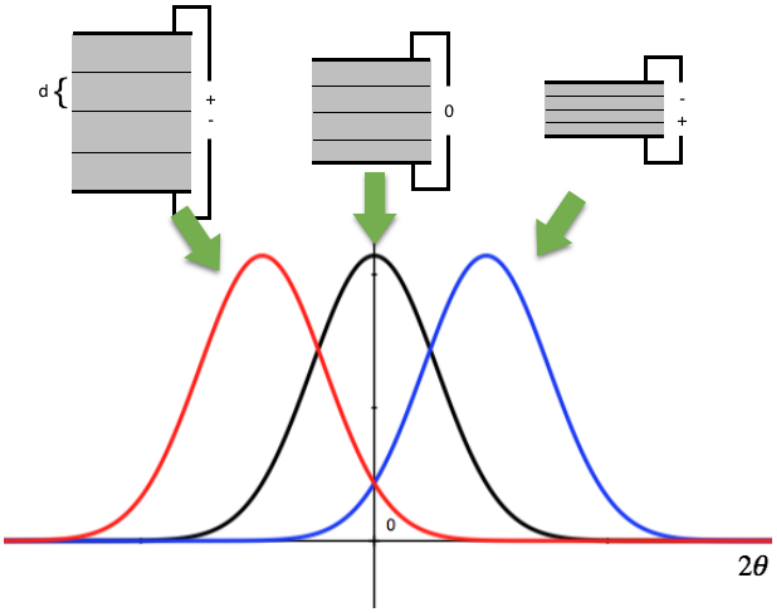

Figure 2.3: Correlation between strain induced changes in interplanar distance d and changes in Bragg-peak positions.

gain all piezoelectric coefficients. G. R. Barsch gives a detailed description on all crystal classes with the respectively associated equations in [9].

2.2 Electrostriction

Next to the converse piezoelectric effect exists electrostriction, which is a universal property in dielectrics and not restricted to non-centrosymmetric lattices. The piezoelectric effect is, as mentioned above, linear and changes its direction of deformation with changing electric field direction. Electrostrictive deformations on the other hand are proportional to the square of the electric field and thus act always in the same direction independent to the electric field direction. This coupling is defined by the following formula [10]:

$$\epsilon_{ij} = q_{ijkl}\, E_k\, E_l \qquad (i,j,k,l = 1,2,3;) \tag{2.16}$$

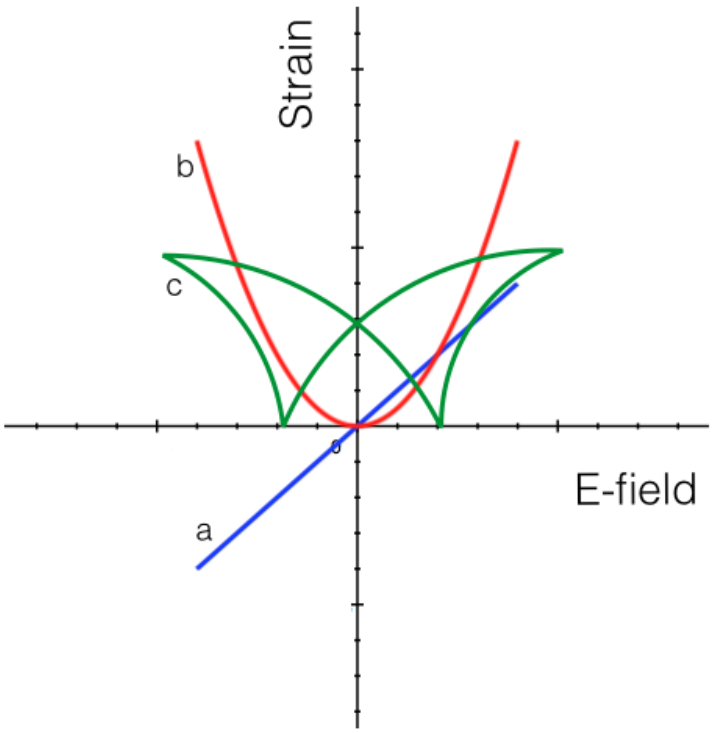

Figure 2.4: Strain vs. external electric field for a) piezoelectric materials in a linear way (blue), b) electrostrictive materials in a squared way (red) and c) ferroelectric materials in a so called butterfly loop (green).

In piezoelectrics, also electrostriction can be present but is usually negligible as it is extremely small. Nevertheless, if electric fields are high enough, the effect can come in the range of a piezoelectric effect. In order to discern which effect one is dealing with, the direction of the external electric field should always be reversed. This way the effects are distinguishable in their behavior on the external electric field. Figure 2.4 gives a comparison of the strain dependence on an electric field for the different effects.

2.3 Ferroelectric and pyroelectric effect

Ferroelectrics are always piezoelectric and pyroelectric but in difference to the effects previously mentioned have ferroelectrics a spontaneous polarization. Pyroelectricity describes the appearance of surface charges through temperature changes on the crystal and is due to the temperature dependence of the spontaneous polarization only. The pyroelectric coefficient γ is therefore the temperature coefficient of the spontaneous polarization [11]:

$$\gamma = \frac{\partial P_s}{\partial T} \tag{2.17}$$

This spontaneous polarization arises from domains with dipoles in the same direction and the sum over these areas defines the net polarization similar to magnetic domains in a ferromagnet. For ferroelectrics these domains are invertible by external electric fields in addition. Figure 2.5 shows a typical hysteresis how it is observed when poling a ferroelectric from one direction to the opposite and back in its first state. With P_r, the remnant polarization without electric field is given, E_c describes the required field to gain a zero polarized material. The strain in the material follows a so called butterfly loop with the external electric field. In figure 2.4 this correlation between strain and electric field is shown not only for ferroelectrics but also for piezoelectrics and the electrostrictive effect described before. Above a temperature dependence of the polarization is mentioned. A critical temperature exists where a phase transition into a paraelectric phase takes place, as long as this temperature is below the materials melting point. These phase transitions can be described in a first approach by Landau theory of phase transitions [12].

2.3.1 Landau theory of phase transitions

In general changes in internal energy can be described by

$$\mathrm{d}U = T\mathrm{d}S + \boldsymbol{\sigma}\mathrm{d}\boldsymbol{e} + \boldsymbol{E}\mathrm{d}\boldsymbol{P} \tag{2.18}$$

with entropy S and the state variables temperature T, electric field E and mechanic stress $\boldsymbol{\sigma}$ acting on a crystal. Gibbs free energy is therefore

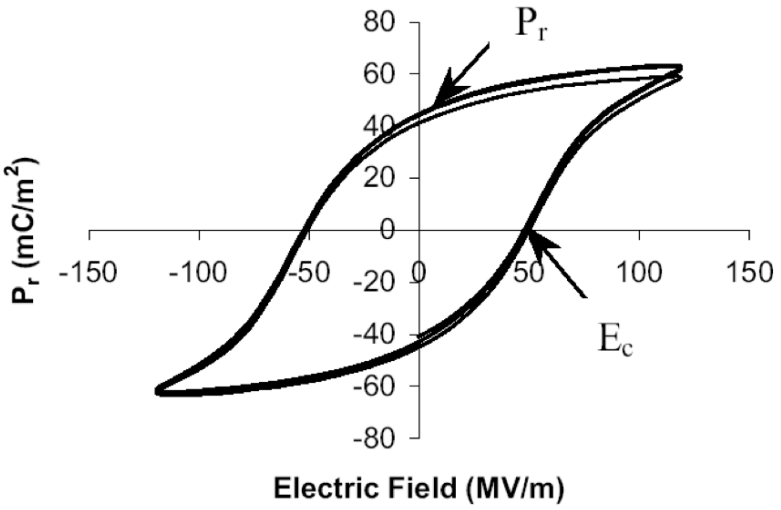

Figure 2.5: Typical hystereses for ferroelectric materials. Plotted is the polarization in the material vs. the external electric field. P_r marks the remnant polarization, E_c the electric field strength at which no polarization occurs. Reprinted from [13]

$$G(T, \boldsymbol{\sigma}, \boldsymbol{E}) = U - TS - \boldsymbol{\sigma e} - \boldsymbol{EP} \tag{2.19}$$

and for the total differential follows

$$\mathrm{d}G(T, \boldsymbol{\sigma}, \boldsymbol{E}) = -S\mathrm{d}T - \boldsymbol{e}\mathrm{d}\boldsymbol{\sigma} - \boldsymbol{P}\mathrm{d}\boldsymbol{E} \tag{2.20}$$

To calculate thermodynamic properties out of this, typically long and numerical intensiv calculations have to be done. Near phase transitions Landau realized that the free energy can be approximated. He coined the concept of an order parameter, which is zero at the high temperature side of the transition and different to zero at the low temperature side. Near the phase transition this order parameter is small and therefore a Taylor expansion of the free energy in this order parameter gives a good approximation. Phase transitions are ordered after Ehrenfest by: A phase transition of n-th order is

1. continuous in its first to (n-1)th derivation

2. discontinuous in its n-th derivation

3. infinity in its (n+1)th derivation

However, phase transitions of 3rd and higher order haven't been shown yet.

As it is a little bit easier in mathematics, Landau theory for second order phase transitions is treated here first. The Taylor expansion for the free energy with order parameter m is

$$f(T) = f_0(T) + \alpha m^2 + \frac{1}{2}\beta m^4 \tag{2.21}$$

$$\text{Landau parameters} : \alpha > 0, \beta > 0$$

β is assumed to be positiv so the free energy has a minimum for finite values of the order parameter. α is greater zero in the case that the order parameter is zero and describes therefore the high temperature phase. At a transition m is finite and α has to change its sign at the critical temperature T_c and below. The following ansatz is made:

$$\alpha = \alpha_0(T - T_c) \tag{2.22}$$

The free energy

$$f(T) = f_0(T) + \alpha_0(T - T_c)m^2 + \frac{1}{2}\beta m^4 \tag{2.23}$$

is shown in figure 2.6. For $T < T_c$ the figure shows two minima in the order parameter.

$$m = \pm\sqrt{\frac{\alpha_0(T_c - T)}{\beta}} \tag{2.24}$$

Choosing the polarization as order parameter for ferroelectrics these minima fit to the fact that a ferroelectric crystal will have a spontaneous polarization in one of two possible directions along a polar axis after a phase transition.

To describe first order phase transitions, the free energy has to be expanded to the sixth order:

$$f(T) = f_0(T) + \alpha_0(T - T_c)m^2 + \frac{1}{2}\beta m^4 + \frac{1}{3}\gamma m^6 \tag{2.25}$$

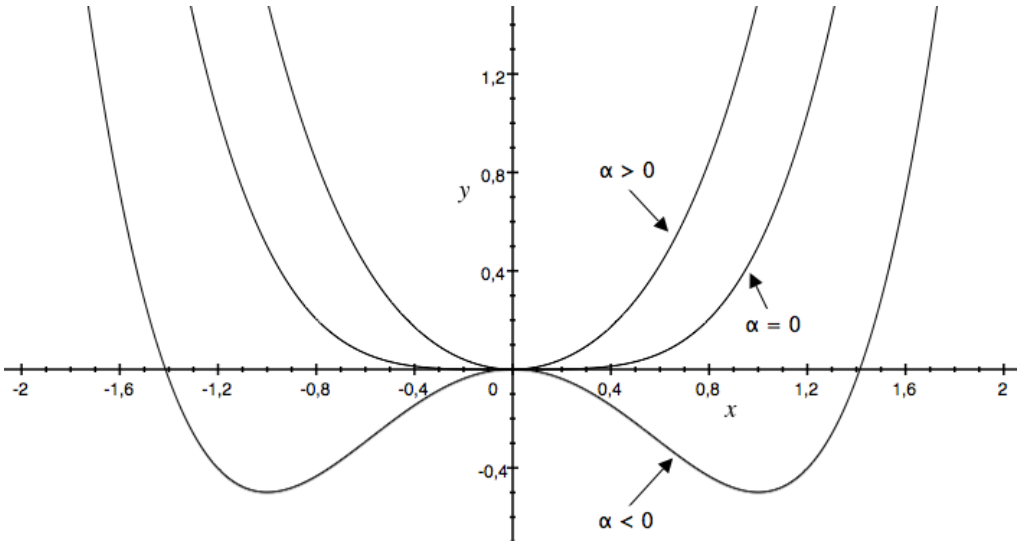

Figure 2.6: Free energy vs. order parameter for different temperatures in Landau theory for second order phase transitions.

$$\alpha_0 > 0, \beta < 0, \gamma > 0$$

Figure 2.7 shows free energy curves for different temperatures around the critical temperature. Again the order parameter minimizes the free energy, and one gets the following solutions for the order parameter:

$$\begin{aligned} m &= \pm\sqrt{\frac{-\beta+\sqrt{\beta^2-4\alpha_0(T-T_c)\gamma}}{2\gamma}} && \text{for} \quad T < T_c \\ m &= 0, \pm\sqrt{\frac{-\beta+\sqrt{\beta^2-4\alpha_0(T-T_c)\gamma}}{2\gamma}} && \text{for} \quad T_c < T < T_1 \\ m &= 0 && \text{for} \quad T_1 < T \end{aligned} \tag{2.26}$$

with T_1 as the point where the two non-zero solutions become unstable:

$$T_1 = \frac{\beta^2}{4\alpha_0\gamma} + T_c \tag{2.27}$$

The jump in the order parameter at T_c is

$$\Delta m = \sqrt{\frac{-\beta}{\gamma}} \tag{2.28}$$

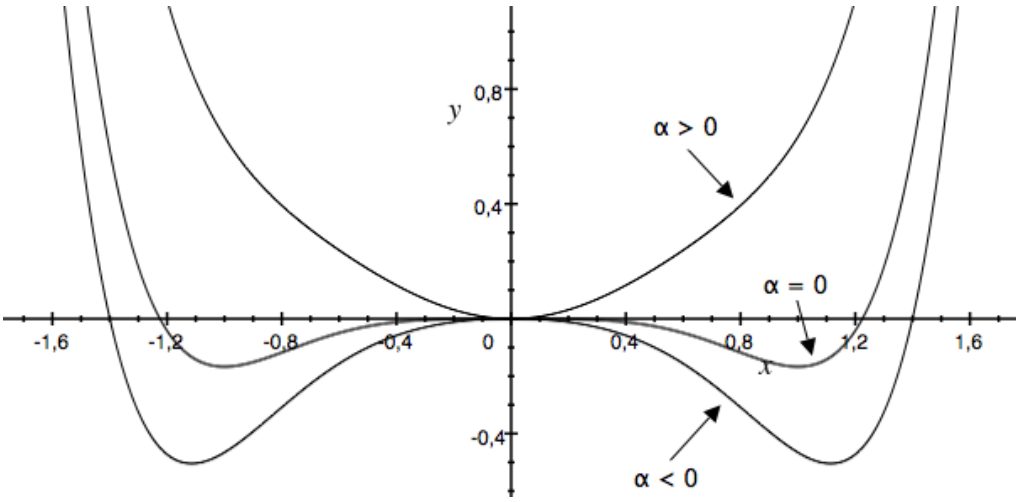

Figure 2.7: Free energy vs. order parameter for different temperatures in Landau theory for first order phase transitions.

while the jump at T_1 is

$$\Delta m = \sqrt{\frac{-\beta}{2\gamma}} \tag{2.29}$$

This means, with the example of a ferroelectric to paraeletric first order phase transition:

- heating up a ferroelectric will cause a phase transition into a paraelectric state at temperature T_1 with a jump in the polarization from a finite value to zero.

- cooling it down it will stay paraelectric until T_c where it undergoes a phase transition to a ferroelectric with a jump in spontaneous polarization to a finite value.

Figure 2.8 shows the difference in polarization vs. temperature for ferroelectrics with second order and for those with first order phase transition.

Figure 2.8: Shape of the spontaneous polarization for ferroelectric materials. A material with a second order phase transition shows a continuous decrease in its polarization until it reaches its critical point, a first order phase transition is marked by a jump in polarization. At the critical points a phase transition from ferroelectric to paraelectric state takes place.

2.4 Thermal expansion

As the main part of experiments in this work aims on detecting changes of Bragg-peaks in diffraction patterns, one has to take thermal expansion into account. In general a material will change its dimensions more or less due to a change in temperature. This leads also to a change in interplanar distances d and because of that will cause a change in a Bragg-peak position. The relation between change in size and change in temperature is described by the linear thermal expansion coefficient α,

$$\alpha = \frac{1}{L}\frac{\mathrm{d}L}{\mathrm{d}T} \tag{2.30}$$

with a specific length L and the rate of change in length per unit change in temperature. Materials which expand in all main directions the same are called isotropic and can be described with the same coefficient in all directions. Anisotropic materials on the other hand have different expansion coefficients for different directions. There are other expansion coefficients to describe a volu-

metric or areal expansion, but for the purpose of this work it is enough to deal with the linear expansion coefficient to describe changes in a certain direction.

Usually the coefficient varies with temperature but for small temperature ranges the equation above can be linear approximated to

$$\Delta L = \alpha L \Delta T \tag{2.31}$$

The connection to an X-ray diffraction pattern is done when L is described as

$$L = \frac{\lambda}{2 \sin \theta} \tag{2.32}$$

L equals therefore the interplanar distance d_{hkl} in the Bragg equation. Thermal expansion can be very different for different materials and as example, figure 2.9 shows a measurement of potassium hydrogen phthalate on silicon at different sample temperatures. This sample is described in chapter 4.2. One can clearly see the different temperature influences on silicon and potassium hydrogen phthalate in differently strong shifting Bragg-peaks. In conclusion it is to say that one has to keep thermal expansion in mind to avoid a distortion of measurements. Changes in Bragg-peak positions due to a piezoelectric effect are very low and if the thermal expansion coefficient has an accurate value, temperature fluctuations of some degree can distort a measurement in a sensible way. Reasons for heat fluctuations can be the X-ray source, which produces a lot of waste heat, or a sample itself which isn´t at thermal equilibrium with the measurement chamber and/or the sample stage.

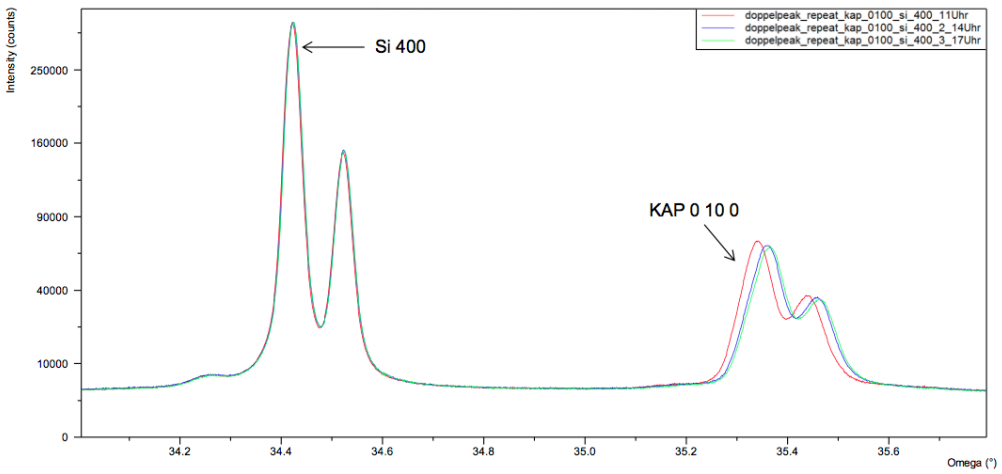

Figure 2.9: Three measurements of potassium hydrogen phthalate on silicon showing the effect of different thermal expansion coefficients and the resulting shift in Bragg-peaks.

2.5 MATLAB peak-fitting

In case of determining piezoelectric constants out of X-ray diffraction patterns, more or less only peak positions are of interest. Nevertheless evaluating hundreds of measurements onto their peak positions by hand seemed to be very ineffective. Therefore a MATLAB script was written to automatically detect peaks in diffraction patterns and determine changes of peak positions in a specific dataset.

Basic concept is fitting the experimental data as a Gaussian curve:

$$y = Ae^{\frac{-(x-\mu)^2}{2\sigma^2}} \tag{2.33}$$

where A marks the height, σ the width and its center position $x = \mu$. By taking the natural logarithm one gets the function of a parabola with the same peak position:

$$\begin{aligned} \ln y &= \ln A - \frac{\mu^2}{2\sigma^2} + \frac{2\mu x}{2\sigma^2} - \frac{x^2}{2\sigma^2} \\ &= a + bx + cx^2 \end{aligned} \tag{2.34}$$

This leads to the possibility to fit a parabola with a,b and c and to determine the peak position by:

$$\mu = \frac{-b}{2c} \tag{2.35}$$

The parabola fit was done using MATLABs fit function 'polyfit'. To avoid errors due to noise, thresholds are set to distinguish between background and a possible peak. Starting from the low angle side, intensity for every point is checked. Is the beginning of a peak found by a certain amount of points above a peak-threshold, all points are taken until they fall again below the set threshold. From these peak points are, starting from the center point, as many selected that the upper third of a peak is covered. This has to be done once by hand for every dataset of a sample because data quality and point density was changing in dependence of measurement setup. For even better results, the fitting was done in an iterative process up to 10 times always starting with the parameters of the previous fit [14].

3 Experimental methods

The main focus of this work was on measurements with the PANalytical Empyrean, a multipurpose X-ray diffractometer. With its fast switchable components it is capable of measuring powders, thin films, nanomaterials and solids. Grazing incidence diffraction for a more detailed sample analysis has been done on a Bruker Discovery D8 and heating measurements combined with electric fields were carried out at synchrotron Elettra Trieste. This chapter will give an overview on each setup used in this work and some basic descriptions about measurement methods.

3.1 PANalytical Empyrean

3.1.1 Setup and Components

Figure 3.1 gives an overall view of the X-ray diffractometer. On the left the X-ray tube and primary beam side move on the θ circle and on the right the secondary beam side and detector move on the 2θ circle. This setup has the advantage of a stationary stage. Also the DC voltage supply, able to deliver up to 230 V, is shown in figure 3.1. A schematic drawing of the beam path is given with figure 3.2.

As X-ray source a water cooled copper tube, powered with 40 mA at 40 kV is used. With different divergence slits reaching from $1/32\,^\circ$ up to $1/2\,^\circ$ and beam masks to adjust the beam to sample size in horizontal direction, the beam shape can be influenced in a fast and easy way. A parallel beam mirror collimates the beam to enable a parallel beam geometry with a divergence below 0.055° and acts as monochromator to get mainly CuK_α radiation with a wavelength of $\lambda = 0.154\,\text{nm}$. An alternative offers the also available Bragg-Brentano geometry,

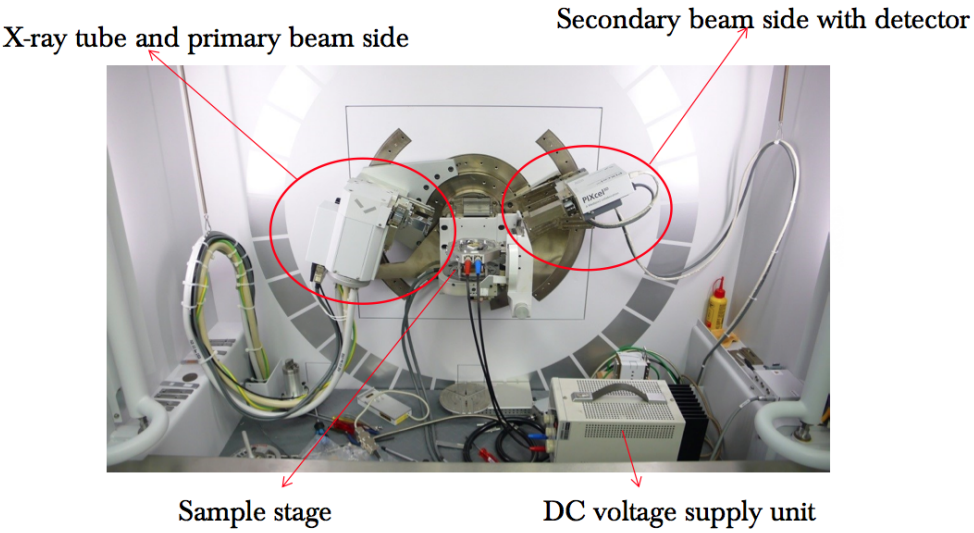

Figure 3.1: Measurement chamber of the Empyrian PANalytical X-ray diffractometer. The electric stage is mounted and connected to a DC voltage supply unit.

which has advantages concerning signal-to-noise ratios or the angular resolution but because of mainly focusing on peak positions the choice fell on the parallel beam mirror which delivers more accurate results at this task as sample alignment in height does not lead to errors so much. Next a programmable beam attenuator protects the detector against too high beam intensity. The attenuator automatically turns a 0.125 mm Ni-plate into the beam path above a specified count rate. In figure 3.2 also the measurement direction and direction of the electric field applied on the samples are drawn. They both point in the same direction, which gives strong limitations in the accesible piezoelectric coefficients. Relating to the matrix in Equation (2.5) only one element with two identical indices is measurable, this is set due to the sample preparation, explained in section 1.2. On the diffracted beam side are an changeable anti-scatter slit and a 0.02 rad soller slit to prevent information from radiation not scattered by the sample.

The $PIXcel^{3D}$ detector is a solid state detector with a pixel matrix of $255 \cdot 255$ channels and a pixel size of $55 \cdot 55\,\mu$m. It can be operated in three different modes:

0D also receiving slit mode; the detector acts like a point detector

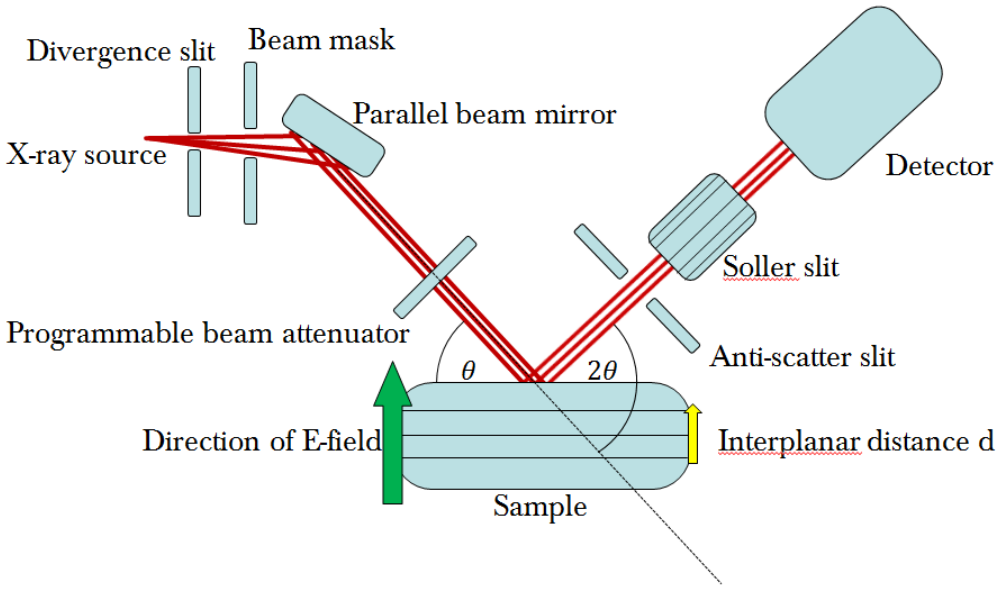

Figure 3.2: Schematic drawing of the beam path in the measurement chamber of the Empyrian PANalytical X-ray diffractometer. Divergence slit, beam mask, beam attenuator and anti-scatter slit are easily changeable between two experiments. Also drawn are the given direction of the external electric field and the direction of measurable interplanar distance d in the sample.

1D also scanning line mode; every horizontal line is read out by it´s own and summed up for a specific 2θ angle

2D reciprocal space maps can be measured as every pixel is read out individually

In every mode one can set the vertical opening by setting the number of used channels. The measurement setup was of utmost importance in order to determine peak positions with smallest possible error. To get a feeling for the different combinations of slits and masks together with detector settings a series of specular scans (see Section 3.1.2) were made on a standard silicon wafer. Figure 3.3 summarizes the five best combinations of slits and detector mode. The curves are labeled with two numbers, first the 2θ position and second the peak full width at half maximum (FWHM). Legend entries have to be read in the following way:

1. used mode of the detector and number of channels
2. used divergence slit on primary beam side
3. used anti-scatter slit on diffracted beam side
4. stepwidth
5. time per step
6. total scan time

The best FWHM value went down to 0.032°, which is only a bit wider than the FWHM of 0.026° measured with a NIST SRM660a LaB_6 standard [15]. The highest intense curve was achieved in receiving slit mode, also it took quite a long time of around 40 minutes, but this mode offers the smallest step size of 0.0001° with a 2θ linearity of $\pm 0.01°$ over the whole angular range. Scanning line mode delivers much faster results but is limited in point density. Nevertheless measurements required individual set ups for every sample to achieve evaluable intensity. To get sufficient statistics a lot of measurements have been done and the analysis under use of standard programs would have taken too much time. Alternatively a $MATLAB$ program was written for detecting peak positions and calculating statistics. The theory to this peak determination ca be found in chapter 2.5.

3.1.2 Specular scans

A specular scan, or symmetric $\theta - 2\theta$ scan is defined by identical angles for the incident and diffracted beam with respect to the interplanar net-planes parallel to the sample surface. This allows to measure the distance d_{hkl} between these net-planes (see figure 3.4). On the PANalytical Empyrean this means that while the primary beam side is moved to change the incident angle of the beam, the secondary beam side is moved with the same speed but opposing direction to hold the diffracted angle equally. The scattering vector $\boldsymbol{q}$ doesn't change its direction, only its length during this measurement. This is the type of scan used to determine piezoelectric constants as it is sensible on deviations of d_{hkl} due to stress or strain.

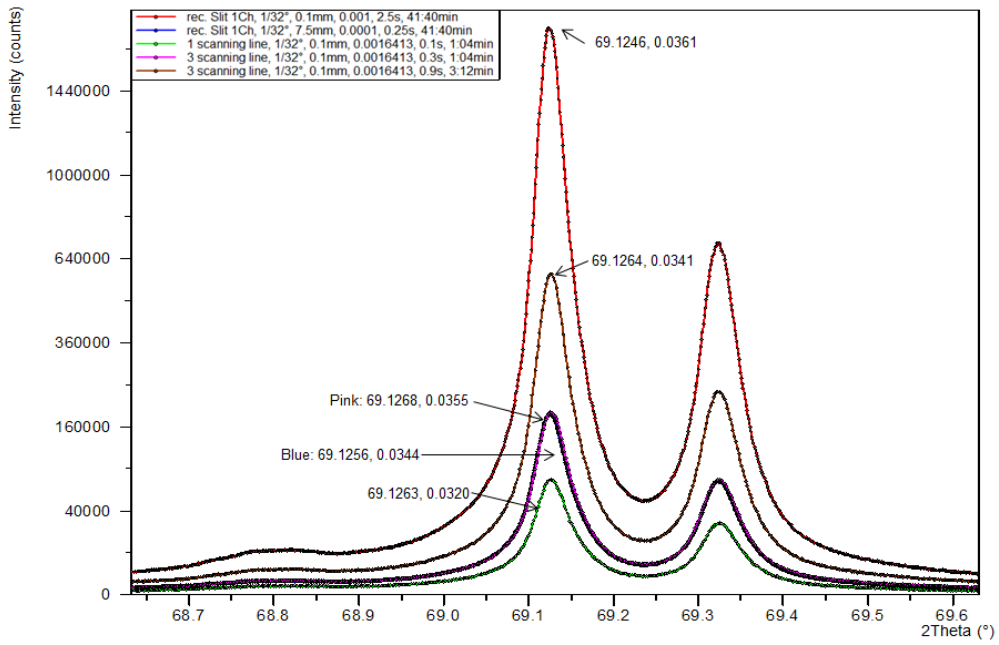

Figure 3.3: Best five measurements of a standard silicon wafer with different combinations of slits, masks and measurement set ups.

3.1.3 X-ray reflectivity

X-ray reflectivity is a method to determine film thicknesses between $2 - 200\,\mathrm{nm}$, film density and roughness. The setup is the same as for a specular scan described above, but accomplished at much lower incident angles around the critical angle θ_c for total external reflection. This angle is for most materials below 0.3° and typical ranges for XRR are between 0° and 5° in θ. Now not interplanar netplanes of crystals reflect the beam, but the surfaces of different layers due to different electron densities. In case of X-rays, the refractive index for solids is below one, resulting in a critical angle below which total reflection occurs. The refractive index can be written as [16, 17]:

$$n = 1 - \delta + i\beta \tag{3.1}$$

with a dispersion term δ

$$\delta = \frac{\lambda^2}{2\pi} r_e \rho_e = \frac{\lambda^2}{2\pi} r_e N_a \rho \frac{Z + f'}{A} \tag{3.2}$$

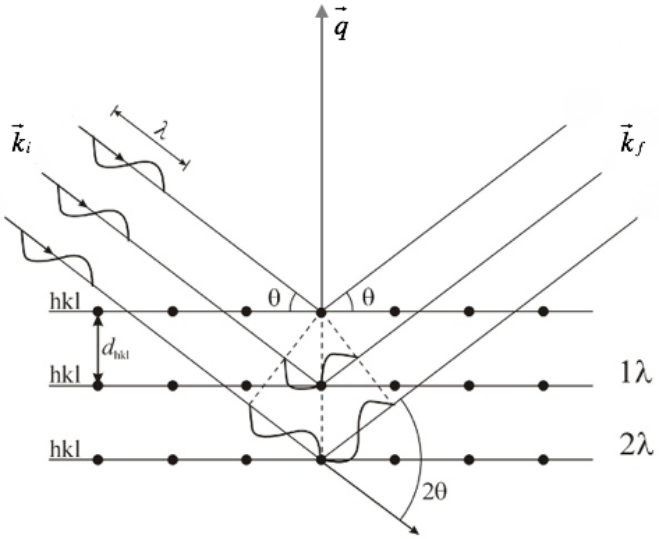

Figure 3.4: Diffraction on a set of net-planes. If the normal of the net-planes divides the angle between incoming and outgoing beam into equal parts, diffraction can occur.

and an absorption term β

$$\beta = \frac{\lambda}{4\pi}\mu_x = \delta\frac{f''}{Z+f'} \tag{3.3}$$

with r_e as classical electron radius, ρ_e the electron density and μ as linear absorption coefficient. N_a is the Avogadro Number, A the atomic mass, ρ the mass density and Z, the number of electrons per atom is expanded by an atomic form factor $Z + f' + if''$, where $f' + if''$ is due to dispersion and absorption. The critical angle can be expressed by

$$\alpha_c = \sqrt{2\delta} \tag{3.4}$$

and is therefore related to the materials density.

Above θ_c reflections occur at top and bottom of the investigated film and interference cause so called Kiessig-fringes. In addition with higher angles, reflected intensity gets lower and the steepness of the curve is related to roughness. The period of the fringes gives information about film thickness t by

$$t = \frac{\lambda}{2\Delta\alpha} \tag{3.5}$$

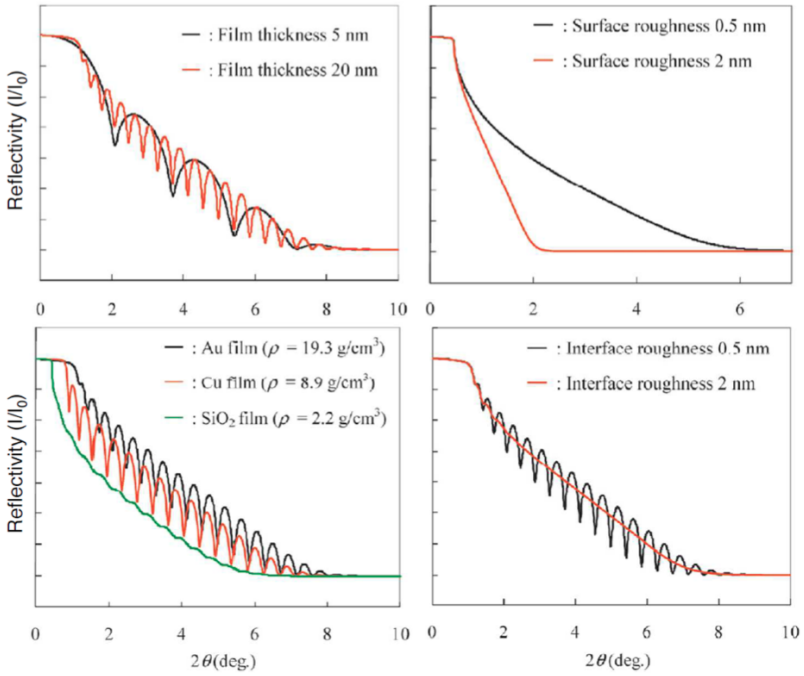

Figure 3.5: Overview of the influences on a XRR measurement by film thickness (top left), surface roughness (top right), materials density (bottom left) and interface roughness (bottom right). Reprinted from [18].

with fringe spacing $\Delta\alpha$. Figure 3.5 gives an overview of the influences on measurement curves by the just mentioned properties of a sample. X-ray reflectivity is explained in more detail by C. Lercher [18].

3.2 Bruker D8

3.2.1 Setup and components

The Bruker Discovery D8 is build up in a geometry to measure lattice planes perpendicular to the sample surface. A picture and schematic drawing is given within figure 3.6. The beam path here runs from right to left. Also here a water cooled X-ray copper tube is used. To be able to perform grazing incidence diffraction the tube is mounted on a Bruker Ultra GID add-on to adjust the in-

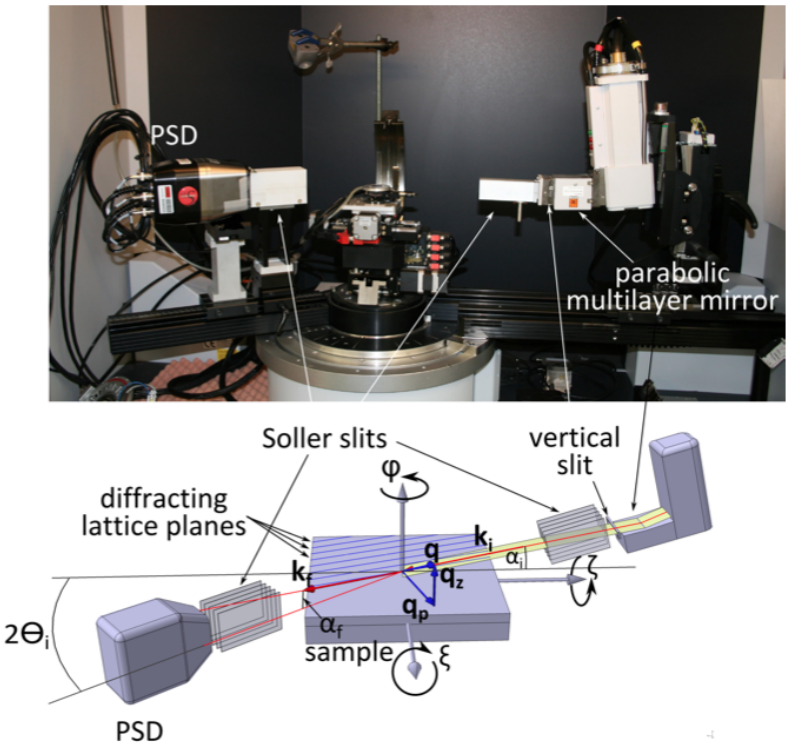

Figure 3.6: Picture and schematic drawing of the Bruker D8. The wave vectors for incident and scattered wave ($\boldsymbol{k}_i$ and $\boldsymbol{k}_f$, respectively) and the corresponding momentum transfer $\boldsymbol{q}$ together with its in-plane and out-of-plane components $\boldsymbol{q}_p$ and $\boldsymbol{q}_z$ are indicated. Reprinted from [20]

cidence angle α_i of the beam with respect to the sample surface. After the tube a Göbel-Mirror collimates the beam to a divergence below 0.025° and monochromatizes it to the wavelength of CuK_α. A primary slit gives the opportunity to limit the beam in height. Last a Soller slit decreases in-plane divergence to 0.35° before the beam hits the sample stage. This is a cradle, moveable around 6 axis to guarantee a perfect alignment. On the diffracted beam side, another soller slit reduces beam divergence to 0.35 °. A position sensitive detector Vantec-1 [19] is used for data collection. It covers an out-of-plane range of $\alpha_f = 7.3°$ with a resolution of $\Delta\alpha_f = 0.007°$. Details on Gracing Incidence X-ray Diffraction can be found at M. Neuschitzer [20].

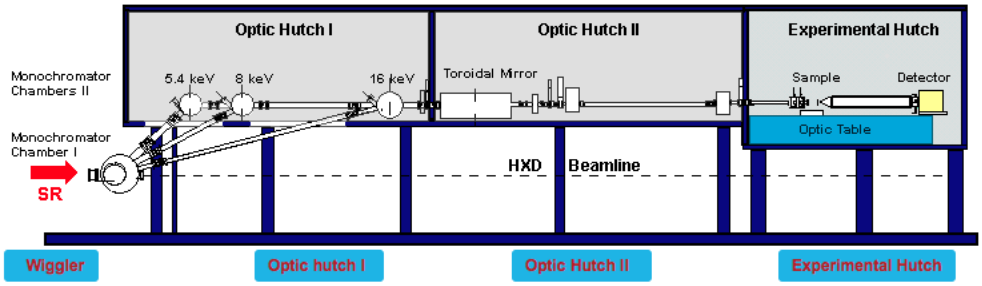

Figure 3.7: Sketch of the high flux SAXS beamline at Elettra Trieste. A 57-pole wiggler serves as source. In Optic Hutch I three monochromators provide a 5.4, 8 or 16 keV strong beam. Optic Hutch II consists a double focusing toroidal mirror. Reprinted from [21]

3.3 Synchrotron Elettra Trieste

The highflux SAXS beamline at Elettra is designed for small angle X-ray scattering (SAXS). Figure 3.7 gives an schematic overview of the beam path. Starting from a 57-pole wiggler as photon source, Optic Hutch I houses three Si(111) flat, asymmetric-cut double crystal monochromators which can be set to fixed energies of 5.4, 8 or 16 keV [22]. Optic Hutch II houses a double focusing toroidal mirror which is fully moveable to get in line with the incoming beam [23]. The Experimental Hutch finally contains the highly variable sample area, space for additional equipment and the detectors. Figure 3.8 shows this hutch with the key components labeled. The sample area allowed to mount the same sample stages and also DC supply unit and heating stage controller were the same as in the home laboratory. A Pilatus 100K detector was used as WAXS detector and mounted in such a way that a 2θ range of roughly 20° from 18° to 38° was covered. The detector has a pixel size of $172 \cdot 172\,\mu m^2$ and an area of $487 \cdot 195$ pixel. To be able to perform heating series under simultaneously applied electric fields, the heating stage was equipped with electric contacts. Figure 3.9 gives a close up on the heating stage with a sample contacted. The high intense beam left a clear to see path on the sample, leading to a breakdown due to material weakening.

The high flux is, on the one hand, a big advantage for measuring times and especially enabled heating series on reasonable time scales. On the other hand one has to be careful about sample degeneration. In our case this limited the possible heating cycles because of the increasing probability of electrical breakdowns.

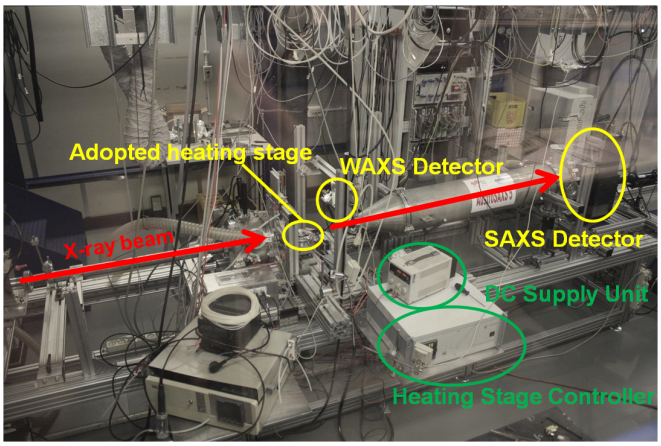

Figure 3.8: Set up of the measurement chamber at Elettra Trieste for wide angle and small angle X-ray scattering. An adopted heating stage with electrical contacts was used.

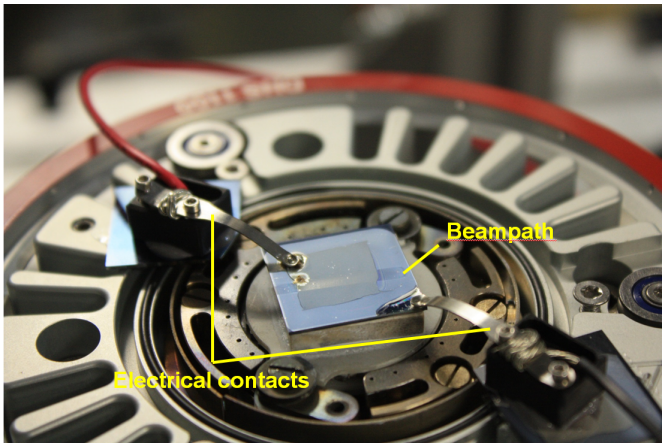

Figure 3.9: Close up on the used DHS 1100 heating stage by Anton Paar at Elettra Trieste. The electric contacts were temporary glued on the outer ring of the heating stage. On the sample the beampath is clearly visible. This sample degeneration over time due to the beam increased the risk of electrical breakdowns during long time measurements.

4 Samples and Results

4.1 Gallium orthophosphate

4.1.1 General information

Gallium orthophosphate ($GaPO_4$) is a trigonal, optically clear crystal similar to quartz (SiO_2). The silicon atoms are substituted by gallium and phosphorus atoms. This leads to piezoelectric constants twice as high as for quartz. Its molecular structure is shown in figure 4.1. The used atomic coordinates are listed in table 4.1 [24]. It crystallizes in the trigonal space group $P3_121$ (No. 152). Unit cell dimensions are $a = 0.4896\,\text{nm}$, $c = 1.1026\,\text{nm}$, $\gamma = 120°$. It must be synthesized as it does not occur naturally. At the moment there is only one Austrian company, *Piezocryst*, who distributes gallium orthophosphate. The material shows no pyroelectricity and is very stable in its piezoelectric coefficients over a big temperature range and therefore often used in high temperature pressure sensors or microbalances. A phase transition into a non-piezoelectric phase occurs at around 970 °C. The piezoelectric constants are as following (given in $10^{-12}\,m/\text{V}$):

$$d = \begin{bmatrix} d_{11} & -d_{11} & 0 & d_{14} & 0 & 0 \\ 0 & 0 & 0 & 0 & -d_{15} & 2d_{11} \\ 0 & 0 & 0 & 0 & 0 & 0 \end{bmatrix}$$

$$d_{11} = 4.5 \qquad d_{14} = 1.9 \tag{4.1}$$

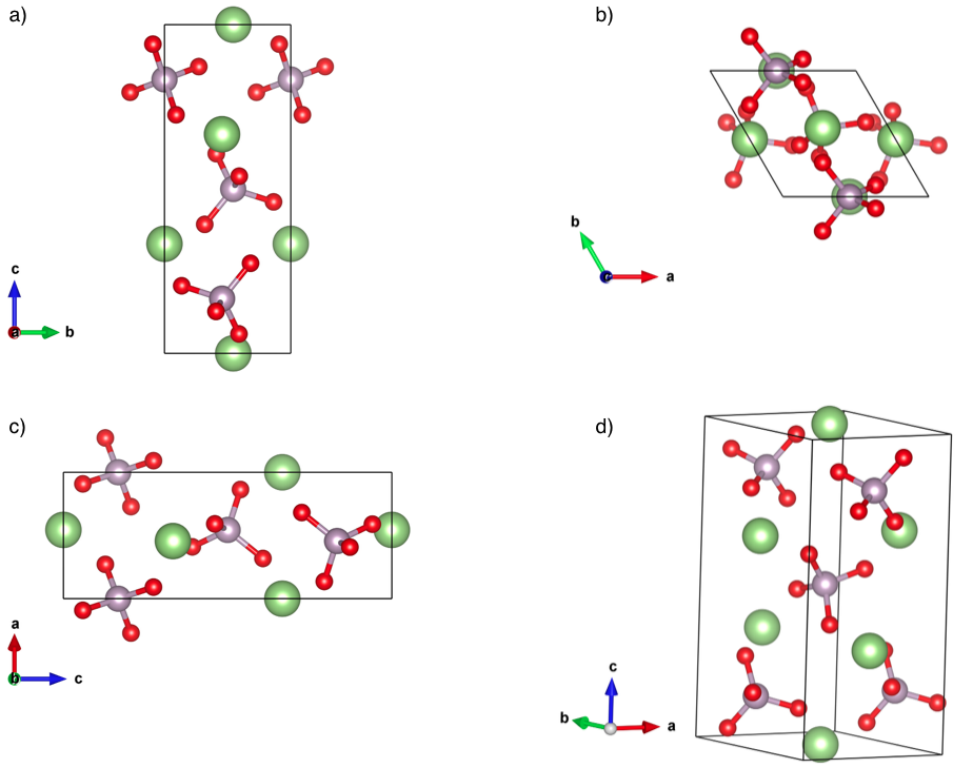

Figure 4.1: Molecular structure of gallium orthophosphate. In red oxygen, purple phosphor and green gallium. a) Projection on the b-c-plane. b) Projection on the a-b-plane. c) Projection on the a-c-plane. d) 3d view.

The material is anisotropic in thermal expansion. At room temperature thermal expansion coefficients are (in $10^{-6}\,\mathrm{K}^{-1}$)

$$\alpha = \begin{bmatrix} \alpha_{11} & 0 & 0 \\ 0 & \alpha_{11} & 0 \\ 0 & 0 & \alpha_{33} \end{bmatrix}$$

$$\alpha_{11} = 12.78 \qquad \alpha_{33} = 3.69 \tag{4.2}$$

Table 4.1: Unit cell and fractional atomic coordinates for trigonal α-quartz-type $GaPO_4$, $P3_121$ [24].

Unit cell		**Fractional atomic coordinates**			
			x	**y**	**z**
a (nm)	0.4896	**Ga**	0.4557	0.0000	0.3333
c (nm)	1.1026	**P**	0.4562	0.0000	0.8333
γ $(^\circ)$	120	$\mathbf{O_1}$	0.4103	0.3185	0.3925
		$\mathbf{O_2}$	0.4080	0.2717	0.8724

The investigated samples are $5 \times 3.3\,\mathrm{mm}$ in dimension and are $0.45\,\mathrm{mm}$ thick. The [110] direction is perpendicular to the surface and equals the direction of measurable interplanar distance d_{hkl}. The samples are already coated on top and bottom with a conductive layer. Figure 4.2 shows the sample stage with a gallium orthophosphate sample on a gold layered silicon wafer. On the right side the gold is contacted and on the opposite the gallium orthophosphate is contacted.

4.1.2 Calculations and results

For measurements a high incident angle should be chosen to make best possible use of the tangent in equation (2.15). Due to the cut of the sample, the highest available peak is the 330 peak at roughly $141^\circ\,2\theta$. Setting the voltage to $200\,\mathrm{V}$ leads with the thickness of the sample to an electric field of

$$E = \frac{U}{d} = 4.4 \cdot 10^5\,\frac{\mathrm{V}}{\mathrm{m}} \tag{4.3}$$

which is far away from the breakdown voltage of about $25 \cdot 10^6\,{}^V/_{\mathrm{m}}$. Equation (2.15) simplifies with measurement direction and direction of the electric field to

$$\begin{aligned} \Delta\theta &= -E \tan\theta (h_1 h_1 e_1 d_{111}) \\ \Delta\theta &= 8 \cdot 10^{-4^\circ} \end{aligned} \tag{4.4}$$

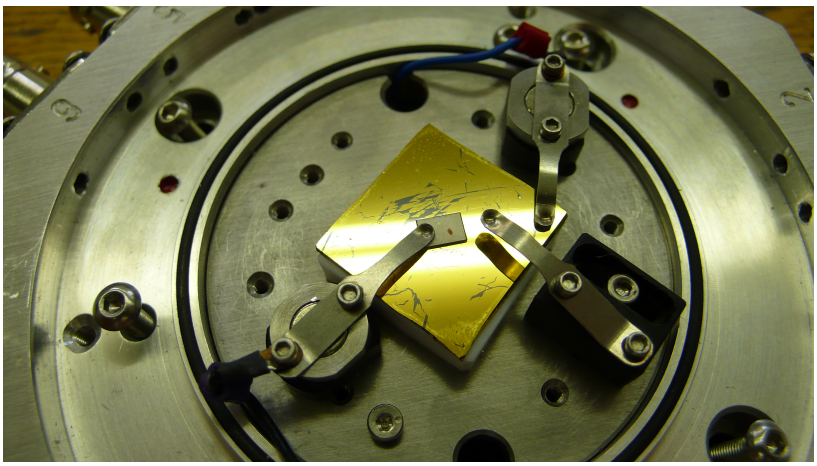

Figure 4.2: Sample stage with contacted gallium orthophosphate placed on a silicon wafer with gold layer

Thermal expansion of gallium orthophosphate is an additional uncertainty. Calculated with equation (2.31), the whole sample expands in direction of measurement by

$$\Delta L = \alpha \, L \, \Delta T = 5.8\,\mathrm{nm} \tag{4.5}$$

upon a temperature fluctuation of $\Delta T = 1°$. This equals a $\Delta\theta$ of $10^{-3°}$ for the 330 peak at 141°.

Two measurement series of gallium orthophosphate have been taken at different voltages from $-230\,\mathrm{V}$ to $+230\,\mathrm{V}$. Series one is shown with figure 4.3. Blue circles indicate a single measurement of the 330 peak, the mean value of 10 measurements for every voltage position is connected by the blue line and the standard deviation is used as error bar. In red the calculated change is indicated. The spread in peak positions for one voltage step is higher than expected but still within the machines 2θ linearity of $\pm 0.01°$. Nevertheless the negative voltage sides mean values agree with the expected piezoelectric shift, on the positive side only the high voltage values run out of line.

A second measurement series was taken with 20 measurements per voltage step (see figure 4.4). Again peak 330 was measured and the same indication applies as in figure 4.3. Also here tendency fits the calculation quite well, also on the

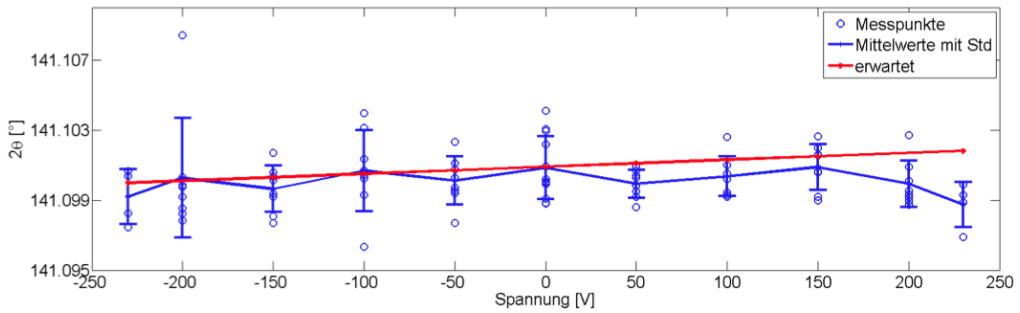

Figure 4.3: Specular scans on $GaPO_4$ at different voltages. Plotted are in blue the Bragg-peak positions from 10 measurements at each voltage point with standard deviation as error bar. Connected by line are the mean values. In red the calculated peak positions.

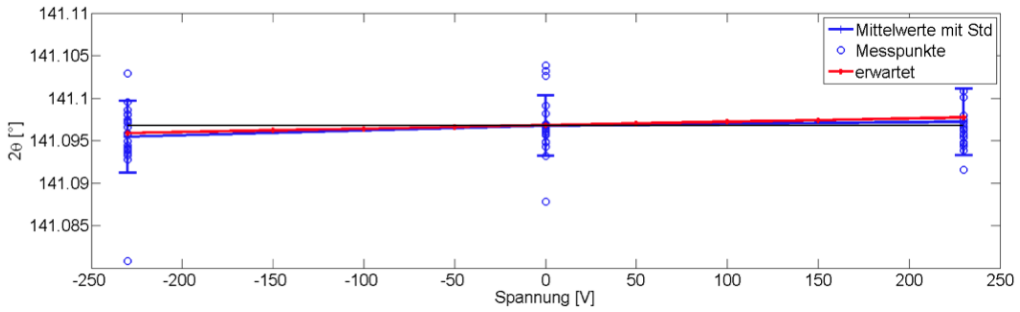

Figure 4.4: Specular scans on $GaPO_4$ at different voltages. Plotted are in blue the Bragg-peak positions from 20 measurements at each voltage point with standard deviation as error bar. Connected by line are the mean values. In red the calculated peak positions.

positive voltage side. On both sides a slight down bending is noticeable. This could be due to an overlapping electrostrictive effect but further investigation was decided not to be useful as it is extremely minute.

In conclusion it is to say that because of the thickness of the sample and the resulting low electric field, the piezoelectric constant d_{11} could not be determined satisfactorily. Its literature value is at $d_{11} = 4.5\,pm/V$ and the evaluated mean value out of the measurements is $d_{11eval} = 14\,pm/V$. Also thermal fluctuations

could have increased the spread in peak positions. Nevertheless, the tendency goes in the right direction, an effect is evident.

4.2 Potassium hydrogen phthalate

4.2.1 General information

Potassium hydrogen phthalate, with the chemical formula $C_8H_5KO_4$, shortened as KAP, belongs to a series of alkali acid phthalates. It is often used in chemistry as standard in calibrating pH-meters for example. It crystallizes in the orthorhombic point group $Pca2_1$ (No. 29) and its unit cell has the dimensions $a = 0.961\,\text{nm}$, $b = 1.385\,\text{nm}$ and $c = 0.646\,\text{nm}$. One unit cell holds four KAP molecules. A unit cell in different views is shown in figure 4.5. The atomic coordinates for the plots are listed in table 4.2 and are taken from Y. Okaya [25]. He reported KAP to be $P2_1ab$ which was converted to $Pca2_1$ [26]. In Figure 4.6 one finds the schematic of one molecule, showing the dipole between the potassium and one oxygen. It grows in {010} platelets which can be seen in figure 4.8, giving a configuration of the molecules in the ab-plane. The polar axis goes down the c-direction. Its morphology is shown in figure 4.7 with the (010) face on top.

One big advantage for our purpose are the factor ten higher piezoelectric constants compared to gallium orthophosphate (given in $10^{-12}\,m/\text{V}$) [27]:

$$d = \begin{bmatrix} 0 & 0 & 0 & 0 & -21.5 & 0 \\ 0 & 0 & 0 & 12.9 & 0 & 0 \\ -46 & 26.5 & 16.5 & 0 & 0 & 0 \end{bmatrix} \tag{4.6}$$

To find out about thermal movement, a heating series was made by measuring the 070 peak at different temperatures from 30 to 90 °C. While figure 4.9 shows the measurements of the peaks, figure 4.10 plots peak position over temperature. Peak shifts are clear to see. Intensity is decreasing minimal, but can be explained as the sample was not realigned between the measurements. The peak positions where fitted linearly:

$$f(x) = p_1 \cdot x + p_2$$
$$p_1 = -0.001963 \qquad p_2 = 47.78 \qquad R^2 = 0.9999 \tag{4.7}$$

With this and with equations (2.31) and (2.32) a thermal expansion coefficient was calculated to a mean value of $\alpha = 38.87 \cdot 10^{-6}\,\text{K}^{-1}$ which is in good agreement with the literature value of $37 \cdot 10^{-6}\,\text{K}^{-1}$ [28].

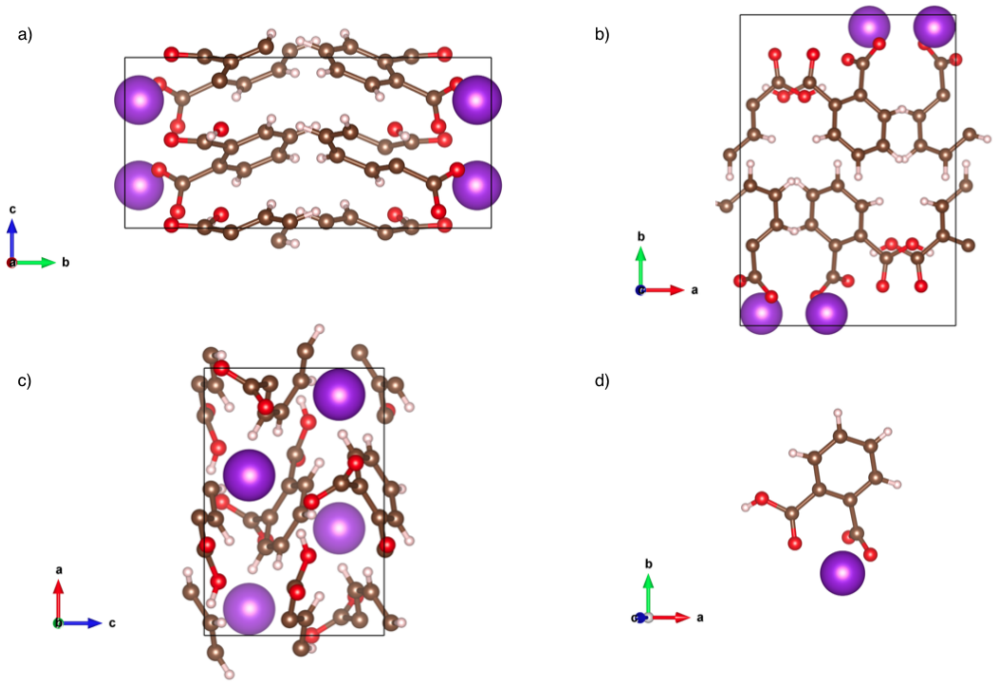

Figure 4.5: Molecular structure of potassium hydrogen phthalate. In red oxygen, in bronze carbon, in white hydrogen and in violet potassium. a) Projection on the b-c-plane. b) Projection on the a-b-plane. c) Projection on the a-c-plane. d) single molecule.

Table 4.2: Unit cell and fractional atomic coordinates for orthorhombic KAP, $Pca2_1$ [25].

	a (nm)	**b** (nm)	**c** (nm)
	0.9609	1.3857	0.6466

Atom	**x**	**y**	**z**
K	0.09898	0.03878	0.25000
C_1	-0.17780	0.21761	0.00561
O_1	-0.29831	0.26258	0.07871
O_2	-0.16109	0.12732	0.01748
C_2	0.06887	0.15685	-0.23842
O_3	0.14522	0.09314	-0.15861
O_4	0.00006	0.14401	-0.40385
C_3	-0.05921	0.28937	-0.02519
C_4	-0.06367	0.38466	0.06263
C_5	0.04731	0.45050	0.03824
C_6	0.16280	0.42058	-0.07350
C_7	0.16928	0.32513	-0.15805
C_8	0.05799	0.25841	-0.13588
H_1	-0.38000	0.23500	0.03800
H_2	-0.14600	0.40000	0.14000
H_3	0.04800	0.52100	0.09600
H_4	0.23700	0.46400	-0.09100
H_5	0.25200	0.30400	-0.23100

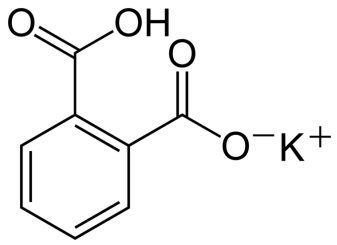

Figure 4.6: Potassium hydrogen phthalate: the potassium (K) makes with the oxygen the dipole for the piezoelectric effect

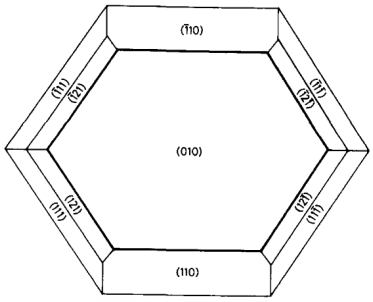

Figure 4.7: Morphology of a potassium hydrogen phthalate crystal [26]

The samples we received were $15 \times 5 \times 0.05\,\mathrm{mm}$ in dimensions and have the (010) plane on top, which is their natural cleavage plane. The long sample side marks the [100] direction, the short side goes along the [001] direction. To be able to guarantee a homogenous electric field inside the samples, a 100 nm aluminum layer was vapor-deposited on top and bottom of the samples. Such a sample already mounted on a gold coated silicon wafer and electrically contacted is shown in figure 4.11. The potassium hydrogen phthalate itself is transparent, on it the aluminum layer can be clearly seen.

4.2.2 Calculations and results

In specular direction accessible were all 0k0 reflections. A list of them is given with table 4.3 including the relative intensity. As one can see, most peaks are

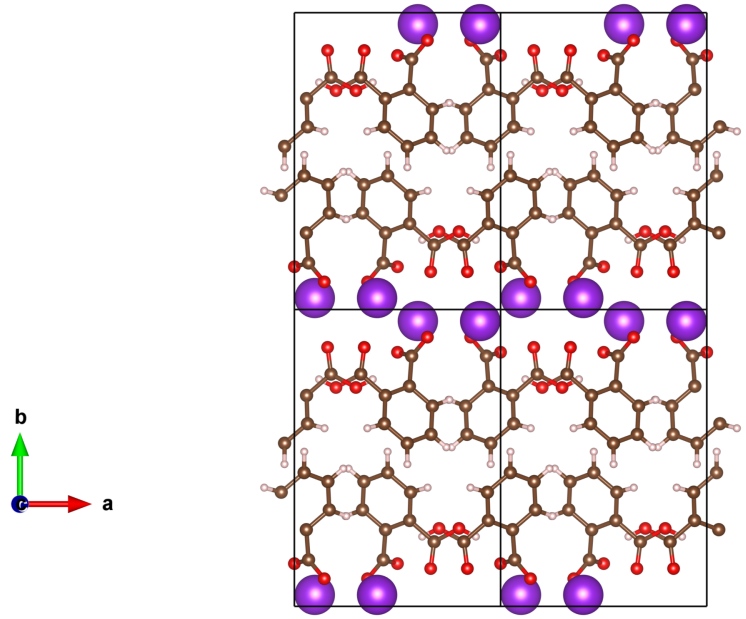

Figure 4.8: Molecular packing of four unit cells of potassium hydrogen phthalate in its ab-plane. The polar axis goes in c-direction.

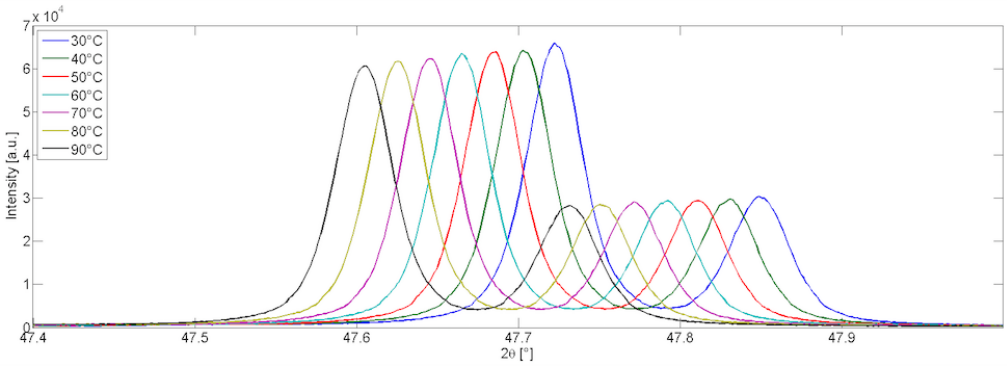

Figure 4.9: In-situ heating experiment to calculate the thermal expansion coefficient of potassium hydrogen phthalate. The 070 Bragg-peak was measured at different temperatures from 30 to 90 degree celsius. In figure 4.10 peak positions vs. temperature are plotted and linearly fitted.

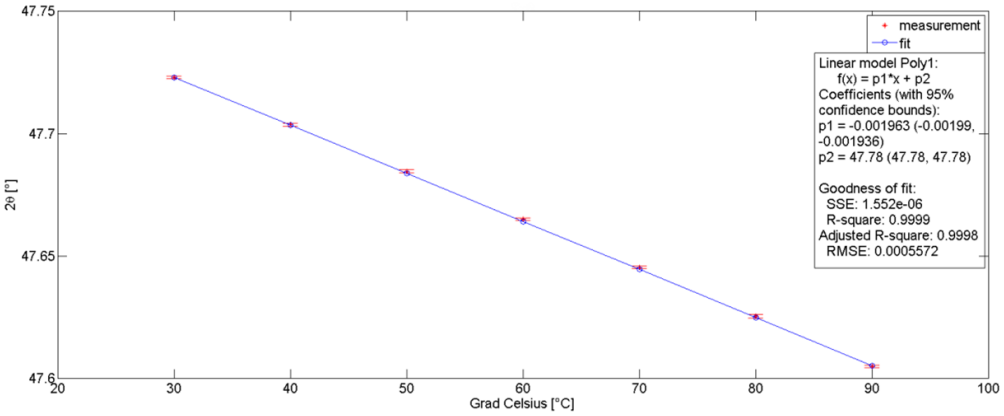

Figure 4.10: Peak positions out of figure 4.9 to calculate the thermal expansion coefficient of potassium hydrogen phthalate. The peak positions are plotted vs. temperature and are linearly fitted.

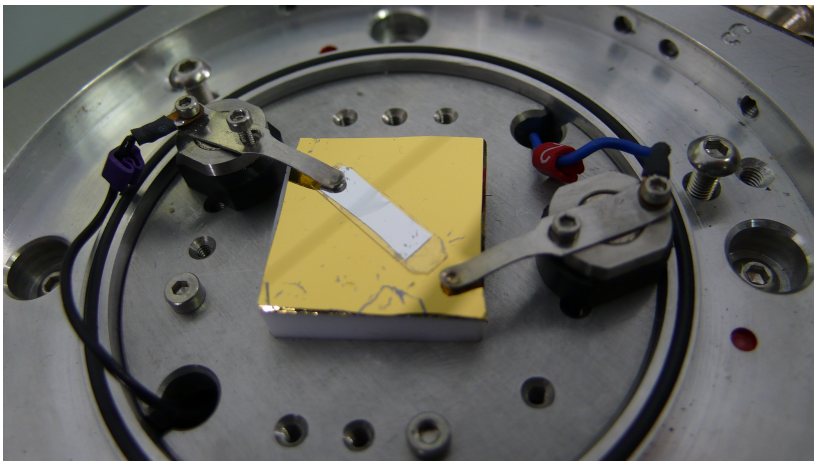

Figure 4.11: sample stage with potassium hydrogen phthalate placed on a silicon wafer with gold layer

Table 4.3: Peak position and intensity for KAP on {010} net planes

H	**K**	**L**	**2θ** (°)	**d** (*nm*)	**I** (*rel.*)
0	1	0	6.626	1.33	100
0	2	0	13.273	0.66	0.97
0	3	0	19.967	0.44	0.04
0	4	0	26.729	0.33	0.00
0	5	0	33.588	0.26	0.41
0	6	0	40.574	0.22	0.58
0	7	0	47.721	0.19	0.99
0	8	0	55.071	0.16	0.05
0	9	0	62.675	0.14	0.11
0	10	0	70.602	0.13	0.34
0	11	0	78.937	0.12	0.18
0	12	0	87.806	0.11	0.12

very weak and so the 070 peak at 47.7° 2θ was chosen as it delivers high enough intensity to hold measurement times short. The 0$\underline{10}$0 peak at 70.6° 2θ was also tested but intensity was too low for a meaningful investigation.

However, there remained a further problem: the samples were cut in the (010) planes. The electric field in [010] direction together with the piezoelectric elements in equation (4.6) results only in a shear strain in yz-direction as only the element d_{24} is nonzero for this electric field vector. Therefore no change in interplanar distance for the 070 Bragg-peak is expected. The consequence of this shear strain is outlined in figure 4.12. On the left side the unit cell in its yz-plane is shown without deformation, on the right side an external electric field is switched on, leading to a shear strain. Marked is furthermore the incident angle θ which will change through the deformation. An applied voltage of 200 V leads to an electric field strength of $4 \cdot 10^6\, V/\mathrm{m}$ and thus to a deformation in incident angle of $\Delta\theta = 0.0008°$. Also this is a quite small change, it corresponds only to the incident angle of the measurement setup when the sample is positioned

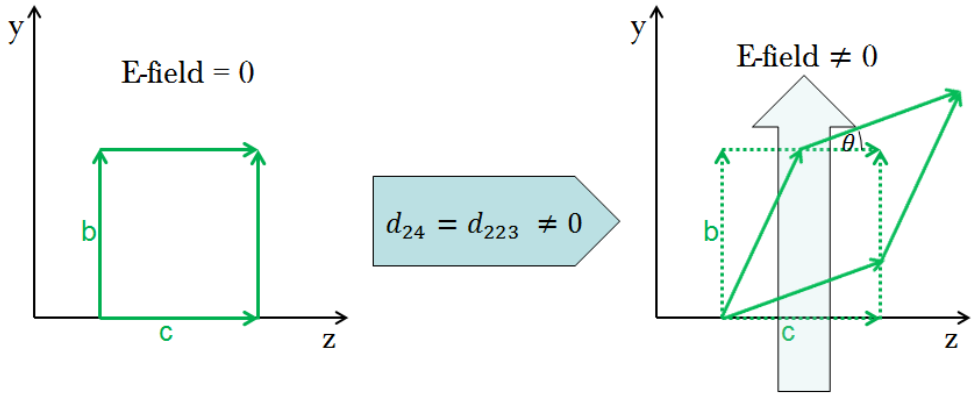

Figure 4.12: Change in the unit cell of potassium hydrogen phthalate due to an external electric field causing a shear strain. On the left the unit cell without electric field, on the right with electric field in y-direction. The shear strain acts in yz-direction.

with its short side in beam direction. This gives the possibility to "turn off" the effect by rotating the sample by 90° such that the long sample side correlates to the beam direction. Then the deformation will correspond to a change in χ angle and will only affect the peak intensity, if any. It was tried to measure this effect and figure 4.13 and figure 4.14 show the results. As well as for gallium orthophosphate, 20 measurements have been taken for every voltage step. Plotted is the mean value and its standard deviation as error at every voltage step. Figure 4.15 compares these two results normed and the measurement with the sample not rotated seems to show a bigger change. Furthermore what immediately catches the eye is the form of the enveloping curve for both plots. An effect much bigger than the calculated one happens and the Bragg-peak shifts always to smaller positions, regardless of the direction of the electric field, which means an expansion of the sample in every case. This could be associated to electrostriction, unfortunately no literature data was found to compare the calculated electrostrictive coefficients. Nevertheless table 4.4 gives a comparison of electrostrictive coefficients for different materials to show that the result is likely

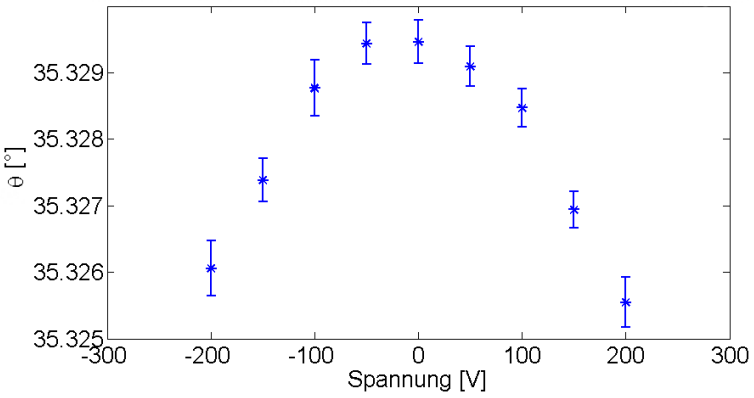

Figure 4.13: Peak positions at different voltages out of rocking curves on potassium hydrogen phthalate. The X-ray beam went in [0 0 1] direction on the sample, the electric field in [0 1 0] direction. Every point represents a mean value out of 20 measurements with their standard deviation as error bar.

to be in the right order of magnitude. Going into detail, one might recognize the bigger errors for the measurement in [100] direction. This can be explained due to the fact that the measurement setup has been the same in both directions for comparison, but the irradiated sample size is much smaller when the sample is rotated with its long side in beam direction. This leads to a worse signal-to-noise ratio and therefore to a bigger spread in peak positions. It was renounced on a more detailed investigation due to this large uncertainty.

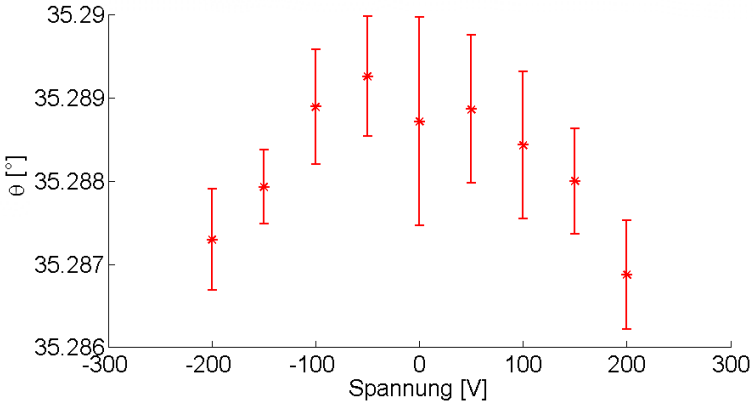

Figure 4.14: Peak positions at different voltages out of rocking curves on potassium hydrogen phthalate. The X-ray beam went in [1 0 0] direction on the sample, the electric field in [0 1 0] direction. Every point represents a mean value out of 20 measurements with their standard deviation as error bar.

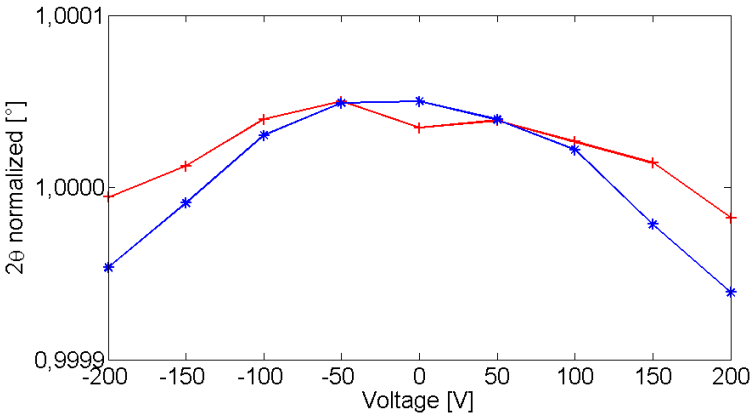

Figure 4.15: Figure 4.13 and figure 4.14 normalized and overlaid for easier comparison.

Table 4.4: Electrostrictive coefficients calculated for KAP out of taken measurements and literature values for Lead-Zirconate-Titanate (PZT), Lead-Magnesium-Niobate (PMN), and PMN-Platinum (PMN-PT).

Material	**Electrostrictive coefficient** $\left(\frac{C^2}{N^2}\right)$
KAP, figure 4.13	-3.17×10^{-16}
KAP, figure 4.14	-5.05×10^{-17}
PZT[1]	-5.32×10^{-23}
PMN[1]	-2.59×10^{-17}
PMN-PT[1]	-2.29×10^{-18}

[1]Literature values out of [29]

4.3 Polyvinylidenfluorid-Trifluoroethylen

4.3.1 General information

Polyvinylidenefluorid (PVDF) with repeating unit $-(CH_2 - CF_2)-$ is a widely used semicrystalline polymer already implemented from chemical over medical to defense industries [31]. It crystallizes in different phases dispersed in amorphous regions in which the degree of crystallinity strongly depends on preparation and thermal treatment history [32]. While the nonpolar α-phase of PVDF is the most stable at room temperature, its copolymer with trifluoroethylene (TrFE) or $-(CHF - CF_2)-$ crystallizes into the polar β-phase at room temperature. The copolymer (see figure 4.16) has a linear structure in which the monomers are regarded to have a random sequence. Figure 4.17 compares the ferroelectric β-phase with the paraelectric α-phase of PVDF. The red arrows indicate the direction of dipoles. Due to the $trans - gauche$ conformation of polymer chains in the paraelectric phase, they cancel out each other, while in ferroelectric $all - trans$ conformation the dipoles sum up to a net polarization. The α-phase can be transformed into a β-phase by poling, drawing or annealing. Different in P(VDF:TrFE), where the additional fluor forces a ferroelectric $all - trans$ con-

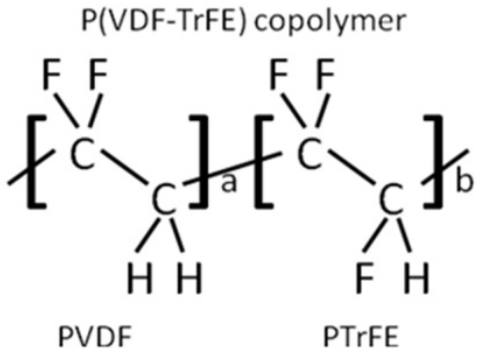

Figure 4.16: Structural formula of P(VDF:TrFE) [30]

figuration already at room temperature (figure: 4.18). Of course VDF to TrFE ratio plays a major role, figure 4.20 shows a phase diagram for different VDF-content. Crystal structures for different phases are given in literature with slight differences, especially for the copolymers. Nevertheless Hasegawa et al. [33] gave reliable values for PVDF, table 4.5 lists them together with lattice parameters for P(VDF:TrFE) 70:30 by Bellet-Amalric and Legrand [34].

4.3.2 Sample preparation

P(VDF:TrFE) 70:30 mol% solved in γ-Butyrolacton (GBL) was used in this work. Samples where prepared by spin coating on Si-wafer with 100 nm silver layer vapor-deposited. After spin coating process, the samples where heated up to 120 °C for 10 minutes to let the solvent evaporate and, in addition, to raise the crystallinity. At this stage, sample thickness was evaluated by XRR measurements and afterwards a 100 nm silver layer was vapor-deposited as top electrode. A finished sample is shown in figure 4.19. Because spin coating did not happen under vacuum respectively transport between spin coating and vapor-deposition, polymer thickness was limited to a lower bound of about 2 μm, otherwise impurities caused short-circuits between the electrodes. Such an impurity was recorded by light-microscopy in figure 4.21. The two silver layers can be seen with some distance due to the polymer in between with a hair like contamination caus-

Table 4.5: Ferroelectric and paraelectric lattice parameters for PVDF and P(VDF:TrFE) 70:30 blend.

	PVDF[1]	**70/30**[2]		**PVDF**[1]	**70/30**[2]
Ferroelectric phase			**Paraelectric phase**		
a (nm)	0.858	0.905	**a** (nm)	0.496	0.986
b (nm)	0.491	0.512	**b** (nm)	0.964	-
c (nm)	0.256	0.255	**c** (nm)	0.462	0.230

[1] [33]

[2] [34]

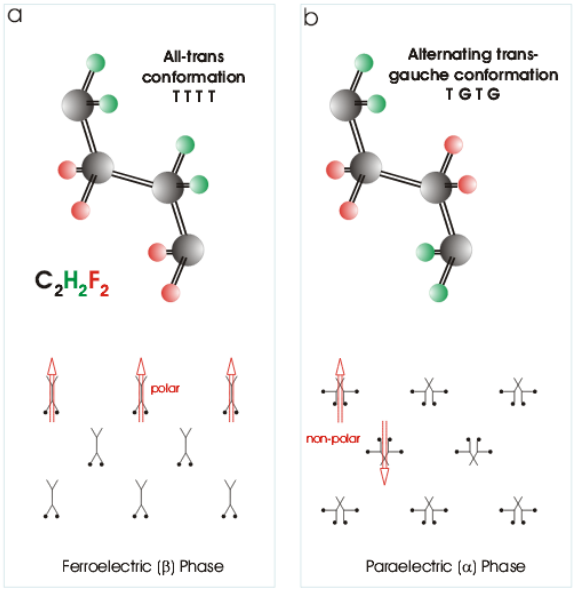

Figure 4.17: Conformations of PVDF for the ferroelectric and paraelectric phase. The red arrows mark the direction of the dipoles. In the paraelectric phase, the dipoles cancel each other out [35].

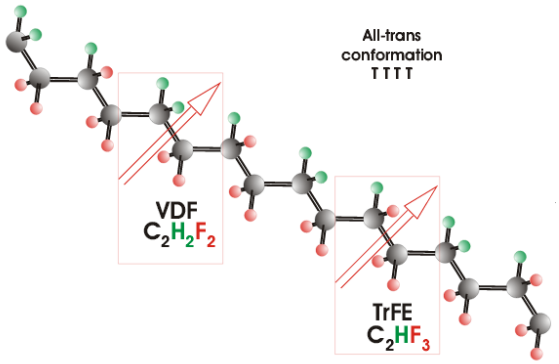

Figure 4.18: Conformation of P(VDF:TrFE) in its ferroelectric state. Red arrows show the direction of the dipoles [35].

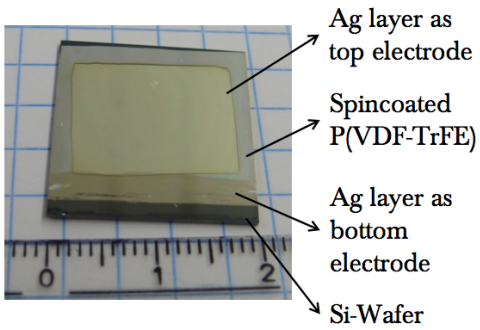

Figure 4.19: Completed sample of P(VDF:TrFE) with silver top and bottom electrode in sandwich configuration on Si-wafer.

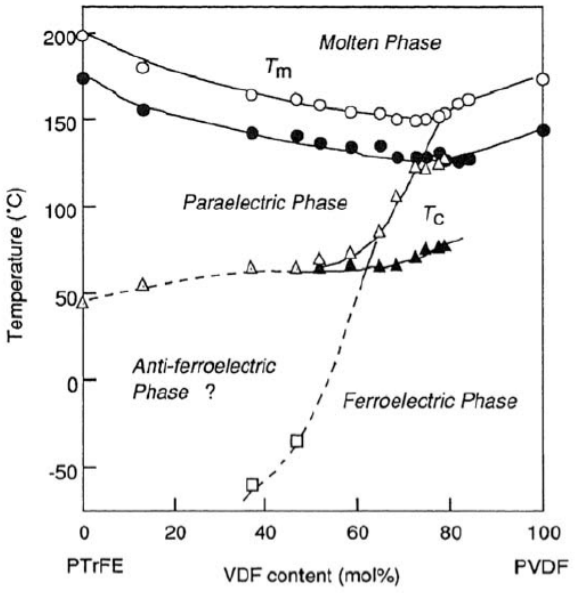

Figure 4.20: Phase diagram for P(VDF:TrFE) with different mixture ratios [36].

ing a direct contact between the two electrodes. Usually, thicknesses of 200 nm and more are not measurable by XRR because of vanishing Kiessig-fringes. The big difference in critical angles for P(VDF:TrFE) and silver on the other hand allowed a thickness determination by fitting only the area between these two critical points. Figure 4.22 compares two XRR measurements, in red a silver coated Si-wafer only, in blue the same sample but with the polymer spin coated on it. The fringes between 1° and 2° are caused by the silver layer only, delivering no information about polymer thickness. But the additional polymer weakens the signal due to its lower critical angle in an area of total reflection for silver. The area in the green circle is zoomed out in figure 4.23. This part of the measurement was fitted (red curve) and delivered a polymer thickness for this sample of 2.342 μm. Table 4.6 gives fitting results in detail. Other samples in this series delivered similar results. It was also tried to verify this thickness by profilometry, but due to the polymers softness, it was easily scratched by the profilometers needle, leading to smaller thicknesses. Such a result sheet is shown in figure 4.24.

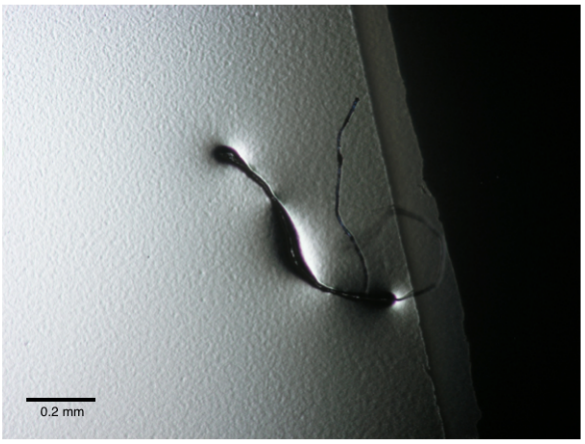

Figure 4.21: Impurity in a P(VDF:TrFE) sample causing a short circuit between the two silver layers.

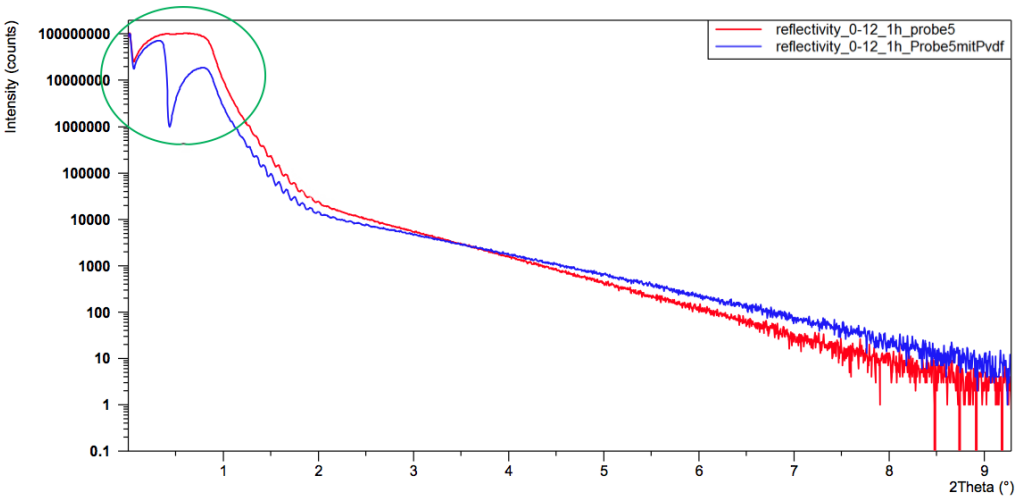

Figure 4.22: X-ray reflectivity measurements on P(VDF:TrFE). Red curve shows a measurement of the lower silver-electrode only, blue curve shows the same sample with P(VDF:TrFE) spin coated on it. The interesting part for a thickness analysis is marked in green.

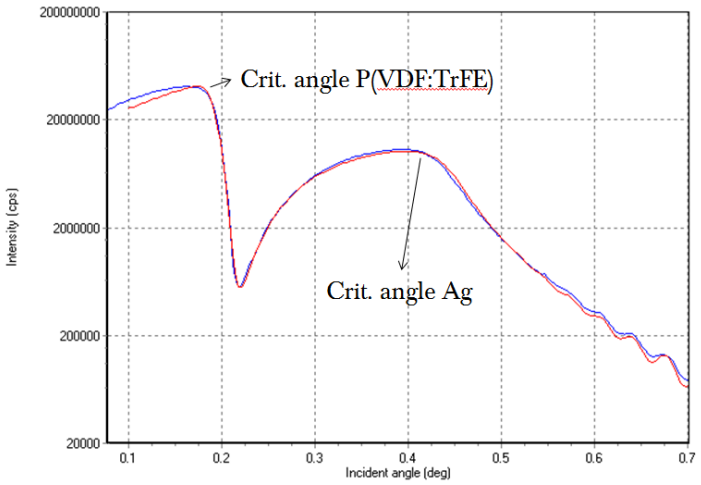

Figure 4.23: X-ray reflectivity measurements on P(VDF:TrFE). The marked part in figure 4.22 is zoomed in here. The critical angles are shown. Blue line shows the measured curve, in red the simulation is shown. Out of the curve shape between the critical angles, the thickness of the spin coated P(VDF:TrFE) was calculated.

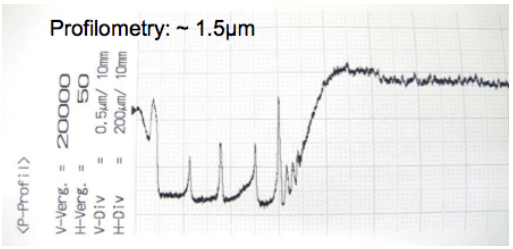

Figure 4.24: Thickness determination of P(VDF:TrFE) by profilometry.

Table 4.6: XRR fitting results for figure 4.23

Layer	**Density** (g/cm^3)	**Thickness** (nm)	**Roughness** (nm)	**Delta, e-7**	**Beta, e-7**
P(VDF:TrFE)	1.733	2342.448	9.057	55.81414	0.24371
Ag	10.508	91.223	1.504	299.02594	24.64807
SiO2	2.100	600000	0.002	67.97208	0.88697

To find out about polymer orientation on the substrate specular scans and GIXD measurements have been made. Figure 4.25 compares measurements with literature data [37]. While the blue GIXD measurement shows the first three accessible peaks, the red specular scan clearly shows an orientation with the 110/200 double peak at 19.9°. This peak is also associated to the ferroelectric β-phase of P(VDF:TrFE), while the paraelectric α-phase can be identified by a 010 peak at 18° [38]. To be sure about the 110/200 double peak, pole figures of P(VDF:TrFE) in its ferroelectric phase have been made at 20° 2θ. They are plotted in figure 4.26 and the integral over ψ is plotted in figure 4.27. The pole figure has been indexed with the lattice parameter of table 4.5, revealing a 110 ring at $\psi = 60°$. This indicates an orientation in direction perpendicular to the substrate but an inplane disorder and matches also the measurements in figure 4.25. For this direction perpendicular to the film surface literature values for the piezoelectric coefficient are given up to $40\,^{pm}/_{\mathrm{V}}$ [39]. Calculating the expected change in $\Delta\theta$ at 200 V with a thickness of 2 μm leads to a change of $\Delta\theta = 0.001°$, which is indeed by a factor 10 higher than the changes for $GaPO_4$ and KAP, but still low because of the very low peak angle of 20°.

4.3.3 Ferroelectric-paraelectric phase transition

Poulsen et al. [40] showed an external electric field dependence of the ferroelectric-paraelectric phase transition temperature at heating and cooling for Langmuir-Blodgett films of the P(VDF:TrFE) 70:30 copolymer. We decided therefore to take a closer look at this phase transition and tried to reproduce these results for our spin coated films. The Curie-temperature for phase transition raises with an increasing external electric field in a linear way:

$$\Delta T_c = \left(\frac{\partial T_c}{\partial E}\right)_p E \tag{4.8}$$

With the coefficients of the Landau-Ginzberg-Devonshire free energy, an adopted theory of the presented Landau-theory in section 2.3.1, and the Clausius-Clapeyron relation [41]

$$\left(\frac{\partial T_c}{\partial E}\right)_p = \frac{1}{\alpha_0}\sqrt{\frac{16\gamma}{3\,|\beta|}} \tag{4.9}$$

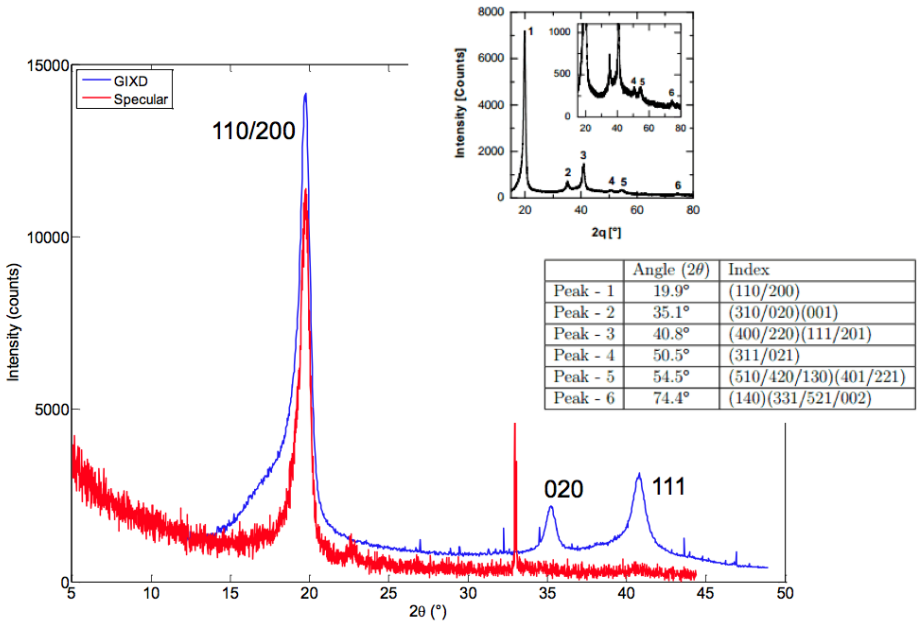

	Angle (2θ)	Index
Peak - 1	19.9°	(110/200)
Peak - 2	35.1°	(310/020)(001)
Peak - 3	40.8°	(400/220)(111/201)
Peak - 4	50.5°	(311/021)
Peak - 5	54.5°	(510/420/130)(401/221)
Peak - 6	74.4°	(140)(331/521/002)

Figure 4.25: Measured and literature data of P(VDF:TrFE). In red a specular scan measured in z-direction, in blue a GIXD measurement in the x-y plane of the sample. In the upper right corner literature measurements and peak positions out of [37].

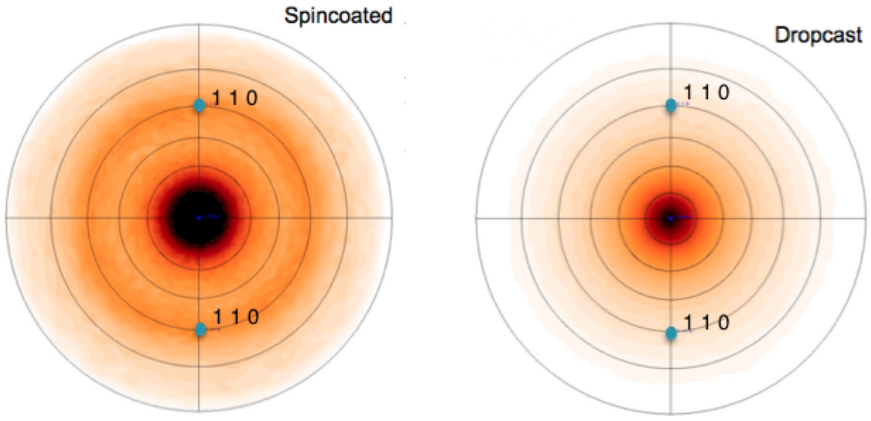

Figure 4.26: Pole figure on P(VDF:TrFE) in its ferroeletric phase at 20° 2θ. Indexed with lattice parameters taken from table 4.5

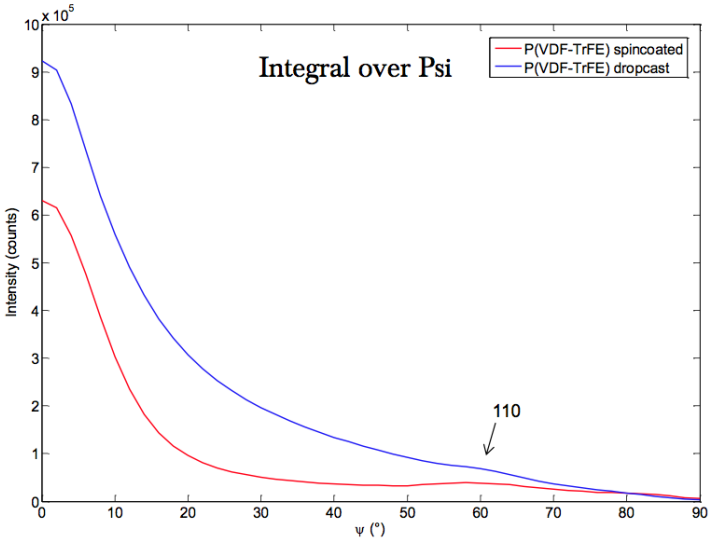

Figure 4.27: Integral over ψ for the pole figures in figure 4.26 showing the 110 rings at 60° more clear.

a theoretical value for this shift can be calculated. Using the coefficients in table 4.7 for P(VDF:TrFE) 70:30 [42] one can calculate a value of $(\partial T_c/\partial E)_p = 2.7 \times 10^{-7}\, Km/\mathrm{V}$. This result is already reduced by 13 %, due to the reducing internal field of the spontaneous polarization.

XRD measurements have been made on the PANalytical Empyrean with a DHS 1100 heating stage by Anton Paar to show the phase transition. Figure 4.28 shows the clear difference of the two phases. In red a peak measured at room temperature, which is clearly associated to the 110/200 double peak at 19.9° of the ferroelectric phase. In blue a measurement at 115 °C, the red peak vanished but another sharp peak at 18° indicates the 010 peak of the paraelectric phase.

Further investigations on this phase transition and its dependence on external electric fields were carried out at Elettra Trieste. A modified heating stage DHS 1100 with additional electric contacts was used (see figure 3.9). These measurements are plotted in figure 4.29. A sample was measured every 10 seconds during heat up with a heating rate of $10\,^{\circ}C/\mathrm{min}$ and during cool down with

Table 4.7: Coefficients of the Landau-Ginzberg-Devonshire free energy and result of the Clausius-Clapeyron relation (4.9) with these coefficients

Coefficient	Value	Unit
α_0	$(7.5 \pm 1.5) \times 10^7$	$\frac{Jm}{C^2K}$
β	$-(1.9 \pm 0.2) \times 10^{12}$	$\frac{Jm^5}{C^4}$
γ	$(1.9 \pm 0.2) \times 10^{14}$	$\frac{Jm^9}{C^6}$
$\left(\frac{\partial T_c}{\partial E}\right)_p$	$(2.7 \pm 0.6) \times 10^{-7}$	$\frac{Km}{V}$

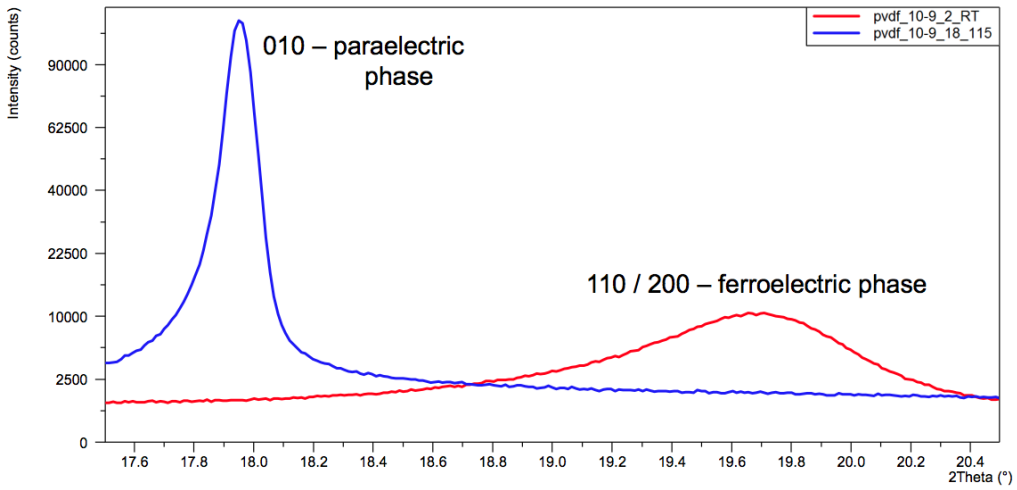

Figure 4.28: Two representative specular scans of P(VDF:TrFE) at different phases. In red the ferroelectric phase at room temperature, in blue the paraelectric phase after heating up to 115 degree celsius.

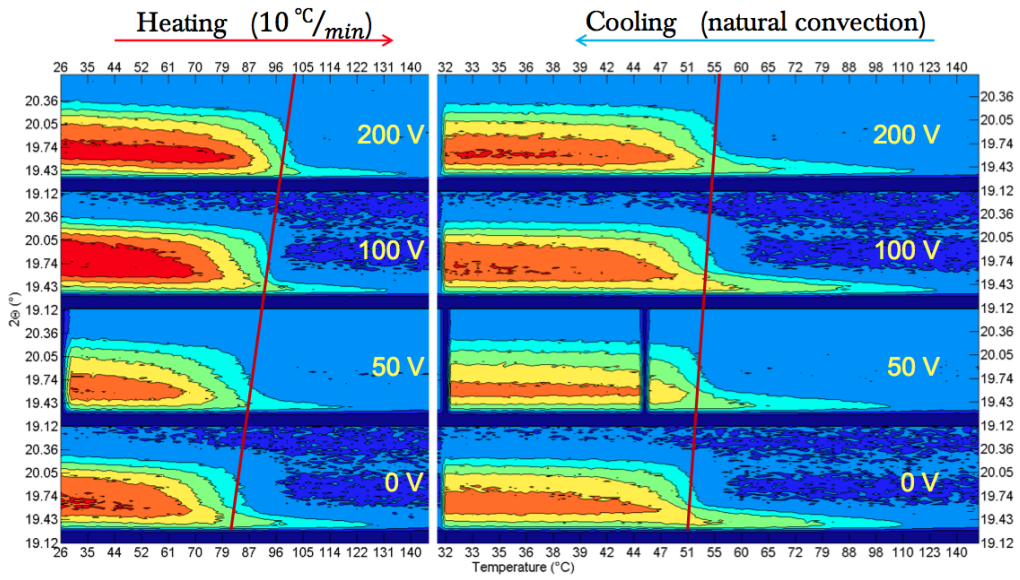

Figure 4.29: Measurements taken at Elettra Trieste plotted as intensity maps (red - high intensity, blue - low intensity). The 110/200 ferroelectric peak at 19.9° was observed. The same heat up and cool down process was measured at four different voltage steps. Indicated with a red line are the points of phase transition.

natural convection by simply switching off the heating stage. This process has been repeated with an applied DC voltage of 50, 100 and 200 V. The WAXS detector was placed in a way to observe the 110/200 peak at 19.9° 2θ. Figure 4.29 shows intensity maps with red indicating high intensity and blue indicating low intensity. Red lines mark the positions of vanishing 110 peaks, indicating a beginning phase transition. As expected, at higher external electric fields the phase transition temperature raises to higher values in both cases, heating and cooling. These transition temperatures are also listed in table 4.8 and plotted in figure 4.30. Rate of increase of this transition temperature with electric field was calculated using the fitted sample thickness of 2.342 μm and compared with the theoretical value and literature data in table 4.9. In addition it is to say that temperature slope in the compared literature is with 1 $^{\circ C}/_{\mathrm{min}}$ much lower than our used slopes.

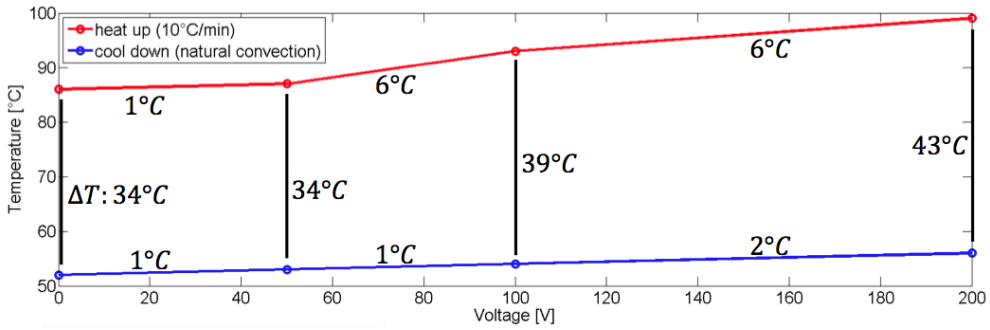

Figure 4.30: Comparison of the results at Elettra Trieste. In red the phase transition temperatures from ferroelectric to paraelectric phase at different voltages while heating up. In blue the phase transition temperatures from paraelectric to ferroelectric phase at different voltages while cooling down. Between to points the temperature difference is given.

Table 4.8: Phase transition temperatures for heat up and cool down process with increasing external electric field from figure 4.29

Voltage (V)	**Temp. heating** $(°C)$	**Temp. cooling** $(°C)$
0	86	52
50	87	53
100	93	54
200	99	56

Table 4.9: Rate of increase of phase transition temperature with electric field calculated from Equation (4.9) and from different measurements.

Source	$\partial T_c/\partial E\ \left(Km/V\right)$
Clausius-Clapeyron relation (Equation (4.9))	$(2.7 \pm 0.6) \times 10^{-7}$
Elettra, cooling	0.5×10^{-7}
Elettra, heating	1.5×10^{-7}
Literature, cooling[1]	$(0.5 \pm 0.2) \times 10^{-7}$
Literature, heating[1]	$(0.4 \pm 0.2) \times 10^{-7}$

[1]Literature data from [40]

One question is left open: the ferroelectric double peak at 19.9° is a composite of the 200 peak at 19.6° and the 110 peak at 19.8°. Due to this closeness they are usually not separable and always measured as one broad peak. However, at all phase transitions in figure 4.29 the 110 peak vanishes while the 200 peak remains much longer. Also at cool down this 200 peak appears much earlier. This behavior was only observed in measurements at the synchrotron while measurements at the PANalytical Empyrean did not reveal such a clear individual behavior. No comparable measurement was found in literature.

5 Conclusion

5.1 Limits of measurability

Piezoelectric constants, usually given in $^{pm}/_{V}$, only cause small changes in interplanar distance d_{hkl}. Equation (2.15) gives the connection to an XRD experiment and let expect changes of some 10^{-4° in 2θ with typical electric field strengths of up to $10^6\,{}^{V}/_{\mathrm{m}}$. While the experimental equipment in principle offers a small enough step size and a high enough resolution, also the tested stage can handle theoretically extremely high voltages as there is no current flowing. But other factors seem to limit the reliability on measured coefficients of such small effects. Samples have to be of high quality to deliver small peaks with a clear peak position. Sample thickness plays an important role if the voltage source is limited. Also to measure all piezoelectric coefficients for a specific material, many samples have to be prepared in different cut directions as XRD is limited in measurement direction and direction of applied electric field. G.R. Barsch [9] gives an overview of measurement and electric field directions to evaluate piezoelectric coefficients for every piezoelectric crystal class. And there are also methods to increase measurement accuracy by applying AC fields for example described by [43]. Nevertheless, XRD measurements on $GaPO_4$ indeed give a piezoelectric value of $d_{11} = 14\,{}^{pm}/\mathrm{V}$, which is three times higher than literature values, but the right tendency is clearly evident. Also the electrostrictive behavior of KAP was measurable and delivered a value of $M_{22} = -5.05 \times 10^{-17}\,{}^{C^2}/\mathrm{N}^2$, which is unfortunately not comparable as no literature value was found to compare with.

A few conditions have to be set to a sample: top and bottom electrode must be attachable to guarantee an equally distributed electric field inside the sample. Sample size has to be big enough to have space for placing the stage electrodes without disturbing the X-ray beam. Besides this, the tested stage is together with

the accuracy of X-ray diffraction a powerful tool for testing the consequence of electric fields on non-conductive samples on their molecular level.

5.2 Combination with heating stage

Investigations on P(VDF:TrFE) revealed another strong combination. The possibility to heat with the heating stage DHS 1100 was expanded by the possibility to apply electric fields. For the ferroelectric-paraelectric phase transition of P(VDF:TrFE) this was used to show a dependence of phase transition temperature due to an electric field. For the phase transition during heat up, this led to a shift in transition temperature of $\partial T_c/\partial E = 1.5 \times 10^{-7}\, Km/\mathrm{V}$. While heating stages are an already common tool in X-ray diffraction, the possibility to apply an electric field on a sample is a desirable extension. Especially at phase transitions many parameters become much larger and therefore impacts due to electric fields are much higher.

But the range of application is not limited to piezoelectric or similar materials. In general, the application of an electric field becomes more and more interesting as a new tuning method. Soft matter like liquid crystals for example are easily influenced by electric fields and in combination with XRD their orientation due to an external electric field can be studied. XRD studies on electric field induced Mott transitions is another example and has been reported by Nakamura et al. [44].

List of Tables

List of Figures

Bibliography

[1] Oxford University Press. http://www.oxforddictionaries.com /definition /english /piezoelectricity.

[2] Will Kleber. *Einführung in die Kristallphysik*. Akademie-Verlag, 1968.

[3] Christian Weißmantel, Claus Hamann, and Hubert Burghardt. *Grundlagen der Festkörperphysik*, volume 2. VEB Deutscher Verlag der Wissenschaften Berlin, 1979.

[4] Peter Hadley. The 32 crystal classes. http://lamp.tu-graz.ac.at/ hadley/ss2/ crystalphysics/crystalclasses/crystalclasses.html.

[5] EN 50324-2 European standard. Piezoelectric properties of ceramic materials and components, part 2: Methods of measurement – low power. Technical report, CENELEC European Committee for Electrotechnical Standardization, 2002.

[6] Jiří Fialka and P Benes. Comparison of methods of piezoelectric coefficient measurement. In *Instrumentation and Measurement Technology Conference (I2MTC), 2012 IEEE International*, pages 37–42. IEEE, 2012.

[7] Charles Kittel. *Einführung in die Festkörperphysik*. Oldenbourg Verlag, 2013.

[8] Antoine Paturle, Heinz Graafsma, H-S Sheu, Philip Coppens, and Pierre Becker. Measurement of the piezoelectric tensor of an organic crystal by the x-ray method: The nonlinear optical crystal 2-methyl 4-nitroaniline. *Physical Review B*, 43(18):14683, 1991.

[9] Gerald R Barsch. X-ray determination of piezoelectric constants. *Acta Crystallographica Section A: Crystal Physics, Diffraction, Theoretical and General Crystallography*, 32(4):575–586, 1976.

[10] JiangYu Li and Nagadip Rao. Micromechanics of ferroelectric polymer-based electrostrictive composites. *Journal of the Mechanics and Physics of Solids*, 52(3):591–615, 2004.

[11] Walter Guyton Cady. *Piezoelectricity. An Introduction to the Theory and Applications of Electrochemical Phenomena in Crystals.* New York, 1946.

[12] L Landau. The theory of phase transitions. *Nature*, 138:840–841, 1936.

[13] M. Zirkl. *Herstellung und Charakterisierung von ferroelektrischen Polymer-Dünnfilmen und ihre Anwendung in integrierten organischen Infrarotsensoren.* PhD thesis, Graz, Univ., Naturwissenschaftliche Fakultät, 2007.

[14] Hongwei Guo. A simple algorithm for fitting a gaussian function. *Streamlining Digital Signal Processing: A Tricks of the Trade Guidebook, Second Edition*, pages 297–305, 2012.

[15] PANalytical. Empyrean, the multi-purpose solution for your analytical needs, 9498 702 20311 pn8484. Technical report, PANalytical B. V., 2009.

[16] Frank Schreiber and Alexander Gerlach. X-ray and neutron reflectivity for the investigation of thin films. *Website. www. physchem. ox. ac. uk/fs.*

[17] Feng Huang. X-ray reflectivity studies of thin films. *The University of Alabama, Tuscaloosa*, 2005.

[18] Christoph Lercher. Surface induced polymorphism of dioctyl-terthiophene on silicon oxide. Master's thesis, Graz University of Technology, 2013.

[19] D. M. Khazins, B. L. Becker, Y. Diawara, R. D. Durst, B. B. He, S.A. Medved, V. Sedov, and T.A. Thorson. A parallel-plate resistive-anode gaseous detector for x-ray imaging. *Nuclear Science, IEEE Transactions on*, 51(3):943–947, June 2004.

[20] Markus Neuschitzer. Grazing incidence in-plane x-ray diffraction on ultra-thin organic films using standard laboratory equipment. Master's thesis, Graz University of Technology, 2012.

[21] https://www.elettra.trieste.it/lightsources/elettra/elettra-beamlines/saxs/beamline.html.

[22] S. Bernstorff, H. Amenitsch, and P. Laggner. High -throughput asymmetric double-crystal monochromator of the saxs beamline at elettra. *J. Synchrotron Rad.*, 5:1215–1221, 1998.

[23] H Amenitsch, S Bernstorff, and P Laggner. High-flux beamline for small-angle x-ray scattering at elettra. *Review of scientific instruments*, 66(2):1624–1626, 1995.

[24] J. Haines, O. Cambon, N. Prudhomme, G. Fraysse, D. A. Keen, L. C. Chapon, and M. G. Tucker. High-temperature, structural disorder, phase transitions, and piezoelectric properties of gapo4. *Phys. Rev. B*, 73:014103, Jan 2006.

[25] Y Okaya. The crystal structure of potassium acid phthalate, kc6h4cooh. coo. *Acta Crystallographica*, 19(6):879–882, 1965.

[26] MHJ Hottenhuis, JGE Gardeniers, LAMJ Jetten, and P Bennema. Potassium hydrogen phthalate: relation between crystal structure and crystal morphology. *Journal of crystal growth*, 92(1):171–188, 1988.

[27] LM Belyaev, GS Belikova, AB Gil'varg, and IM Sil'vestrova. The growth of potassium hydrogen phthalate crystals and their optical, piezoelectric, and elastic properties. *Sov. Phys. Crystallogr*, 14:544–549, 1970.

[28] S Haussühl. Physical properties of phthalic acid and of eight salts of phthalic acid with monovalent cations. *Zeitschrift für Kristallographie*, 196(1-4):47–60, 1991.

[29] Tatsuya Izumi, Manabu Hagiwara, Takuya Hoshina, Hiroaki Takeda, and Takaaki Tsurumi. Analysis of vibration waveforms of electromechanical response to determine piezoelectric and electrostrictive coefficients. *Ultrasonics, Ferroelectrics and Frequency Control, IEEE Transactions on*, 59(8):1632–1638, 2012.

[30] Ronald CG Naber, Cristina Tanase, Paul WM Blom, Gerwin H Gelinck, Albert W Marsman, Fred J Touwslager, Sepas Setayesh, and Dago M De Leeuw. High-performance solution-processed polymer ferroelectric field-effect transistors. *Nature Materials*, 4(3):243–248, 2005.

[31] SB Lang and DK Das-Gupta. Handbook of advanced electronic and photonic materials and devices vol 4 (san diego, ca: Academic). 2001.

[32] MA Barique and H Ohigashi. Annealing effects on the curie transition temperature and melting temperature of poly (vinylidene fluoride/trifluoroethylene) single crystalline films. *Polymer*, 42(11):4981–4987, 2001.

[33] Ryozo Hasegawa, Yasuhiro Takahashi, Yozo Chatani, and Hiroyuki Tadokoro. Crystal structures of three crystalline forms of poly (vinylidene fluoride). *Polymer Journal*, 3(5):600–610, 1972.

[34] E Bellet-Amalric and JF Legrand. Crystalline structures and phase transition of the ferroelectric p (vdf-trfe) copolymers, a neutron diffraction study. *The European Physical Journal B-Condensed Matter and Complex Systems*, 3(2):225–236, 1998.

[35] Yun Luo. *Functional Nanostructures by Ordered Porous Templates*. PhD thesis, Thesis, 2005.

[36] Takeo Furukawa. Ferroelectric properties of vinylidene fluoride copolymers. *Phase Transitions: A Multinational Journal*, 18(3-4):143–211, 1989.

[37] Nitin Shingne. *Morphology and crystal orientation of ferroelectric P (VDF-ran-TrFE) nanostructures in porous aluminium oxide*. PhD thesis, Halle (Saale), Martin-Luther-Universität Halle-Wittenberg, Diss., 2011, 2011.

[38] Andrew J Lovinger, GT Davis, T Furukawa, and MG Broadhurst. Crystalline forms in a copolymer of vinylidene fluoride and trifluoroethylene (52/48 mol%). *Macromolecules*, 15(2):323–328, 1982.

[39] AV Bune, Chuanxing Zhu, Stephen Ducharme, LM Blinov, VM Fridkin, SP Palto, NG Petukhova, and SG Yudin. Piezoelectric and pyroelectric properties of ferroelectric langmuir–blodgett polymer films. *Journal of applied physics*, 85(11):7869–7873, 1999.

[40] Matt Poulsen, AV Sorokin, Shireen Adenwalla, Stephen Ducharme, and VM Fridkin. Effects of an external electric field on the ferroelectric-paraelectric phase transition in polyvinylidene fluoride-trifluoroethylene copolymer langmuir–blodgett films. *Journal of Applied Physics*, 103(3):034116–034116, 2008.

[41] Malcolm E Lines and Alastair M Glass. *Principles and applications of ferroelectrics and related materials*. Oxford University Press, 1977.

[42] Stephen Ducharme, V. M. Fridkin, A. V. Bune, S. P. Palto, L. M. Blinov, N. N. Petukhova, and S. G. Yudin. Intrinsic ferroelectric coercive field. *Phys. Rev. Lett.*, 84:175–178, Jan 2000.

[43] ANTOINE Paturle, HEINZ Graafsma, J Boviatsis, A Legrand, R Restori, P Coppens, Å Kvick, and RM Wing. The influence of an external electric field on the x-ray scattering of 2-methyl-4-nitroaniline, an organic crystal with nonlinear optical properties. *Acta Crystallographica Section A: Foundations of Crystallography*, 45(6):fc25–fc28, 1989.

[44] Fumihiko Nakamura, Mariko Sakaki, Yuya Yamanaka, Sho Tamaru, Takashi Suzuki, and Yoshiteru Maeno. Electric-field-induced metal maintained by current of the mott insulator ca2ruo4. *Sci. Rep.*, 3, 08 2013.

Take from our souls the strain
and stress . . .

(WHITTIER)